

Multi-dimensional and long-term time series monitoring and early warning of landslide hazard with improved cross-platform SAR offset tracking method

YIN YuePing¹, LIU XiaoJie^{2,3*}, ZHAO ChaoYing^{2,4}, TOMÁS Roberto³, ZHANG Qin^{2,4},
LU Zhong⁵ & LI Bin⁶

¹ China Institute of Geo-environment Monitoring, Beijing 100081, China;

² School of Geological Engineering and Geomatics, Chang'an University, Xi'an 710054, China;

³ Department of Civil Engineering, University of Alicante, Alicante 03080, Spain;

⁴ Key Laboratory of Western China's Mineral Resources and Geological Engineering, Ministry of Education, Xi'an 710054, China;

⁵ Roy M. Huffington Department of Earth Sciences, Southern Methodist University, Dallas TX 75275, USA;

⁶ Institute of Geomechanics, Chinese Academy of Geological Sciences, Beijing 100081, China

Received November 13, 2021; accepted February 8, 2022; published online July 11, 2022

Multi-dimensional, long-term time series displacement monitoring is crucial for generating early warnings for active landslides and for mitigating geohazards. The synthetic aperture radar (SAR) interferometry method has been widely applied to achieve small-gradient landslide displacement monitoring; however, measuring the landslide displacement with a steep gradient has posed certain challenges. In comparison, the SAR offset tracking method is a powerful tool for mapping large-gradient landslide displacement in both the slant-range and azimuth directions. Nevertheless, there are some limitations in the existing SAR offset tracking approaches: (i) the measurement accuracy is greatly reduced by the extreme topography relief in high mountain areas, (ii) a fixed matching window from expert experience is usually adopted in the calculation of cross-correlation, (iii) estimating the long-term displacements between the SAR images from cross-platforms and with longer spatiotemporal baselines is a challenging task, and (iv) it is difficult to calculate the three-dimensional (3D) landslide displacements using a single SAR dataset. Additionally, only a few studies have focused on how to realize early warning of landslide deformation using SAR measurements. To address these issues, this paper presents an improved cross-platform SAR offset tracking method, which can not only estimate high-precision landslide displacements in two and three dimensions but also calculate long-term time series displacements over a decade using cross-platform SAR offset tracking measurements. Initially, we optimize the traditional SAR offset tracking workflow to estimate high-precision ground displacements, in which three improvements are highlighted: (i) an “ortho-rectification” operation is applied to restrain the effect of topography relief, (ii) an “adaptive matching window” is adopted in the cross-correlation computation, and (iii) a new strategy is proposed to combine all the possible offset pairs and optimally design the displacement inversion network based on the “optimization theory” of geodetic inversion. Next, robust mathematical equations are built to estimate the two-dimensional (2D) and 3D long-term time series landslide displacements using cross-platform SAR observations. The M-estimator is introduced into the 2D displacement inversion equation to restrain the outliers, and the total least squares criterion is adopted to estimate the 3D displacements considering the random errors in both the design matrix and observations. We take the Laojingbian landslide, Wudongde Reservoir Area (China), as an example to demonstrate the proposed method using ALOS/PALSAR-1 and ALOS/PALSAR-2 images. The results reveal that the proposed method significantly outperforms traditional methods. We also retrieve the movement direction of each pixel of the Laojingbian landslide using the proposed method, thus allowing us to understand the fine-scale landslide kinematics. Finally, we capture and analyze the acceleration characteristics of the landslide, perform an early warning of hazard, and forecast the future displacement evolution based on the 3D displacement time series coupled with the physical models of the rocks.

*Corresponding author (email: 2018026010@chd.edu.cn)

landslide, multi-dimensional displacement, displacement forecasting, early warning, SAR offset tracking

Citation: Yin Y P, Liu X J, Zhao C Y, et al. Multi-dimensional and long-term time series monitoring and early warning of landslide hazard with improved cross-platform SAR offset tracking method. *Sci China Tech Sci*, 2022, 65, <https://doi.org/10.1007/s11431-021-2008-6>

1 Introduction

Landslides are major natural hazards that result in thousands of casualties and property damages worth tens of billions of United States dollar every year [1]. Thus, monitoring the displacements of active slopes for investigation, early warning, and mitigation of landslide hazards is of great research significance [2,3]. Due to its all-weather and large spatial coverage capability, interferometric synthetic aperture radar (InSAR) has been extensively used to detect and monitor landslide hazards [4,5]. InSAR can quantify landslide displacements along the line-of-sight direction with a spatial resolution of meters to tens of meters and an accuracy of a centimeter to millimeter scale under favorable conditions. However, the conventional InSAR method suffers from the limitation of rapid decorrelation in areas with dense vegetation and large-gradient displacements, thus restricting its application to the mapping of slow-moving landslides (i.e., displacement rates slower than ~ 1 m/year) with sparse vegetation [3,6]. When landslide movement is too fast to be measured by InSAR methods, the SAR offset tracking (also sometimes known as sub-pixel image correlation) method offers an alternative method [2,7]. This method measures ground displacement by cross-correlating two images based on the amplitude information and provides two-dimensional (2D) displacement measurements in both the azimuth and slant-range directions with an accuracy of approximately $1/10$ – $1/30$ pixels [8,9]. Currently, various SAR offset tracking methods, such as PO-SBAS [8], PTOT [10], and SPOT-CR [6], have been developed to monitor large ground displacements associated with glacier movements [11], earthquakes [12], underground mining [9,13], and landslide activity [14–16], among others.

However, there are still some shortcomings in existing SAR offset tracking approaches, particularly in terms of characterizing long-term (>10 years) landslide displacements with slow movement velocity (the magnitude of sub-meter to meter scale per year) in areas with steep topography and dominated by distributed scatterers. Thus, the traditional workflow for SAR offset tracking measurements must be improved. First, extreme topography relief in the high mountains can lead to pixel misalignments between the primary and secondary SAR images [17], thus raising severe systematic offset errors in the displacement results. A critical step is to remove topographic offset errors to accurately estimate landslide displacements. Most of the existing studies [2,18] restrain such errors by setting the thresholds of the

spatiotemporal baselines (i.e., long temporal baseline and short spatial baseline or short spatiotemporal baselines). Consequently, the number of offset pairs is often limited by the SAR images obtained from previous satellites, such as ALOS/PALSAR-1. In comparison, seasonal or annual offset pairs are of significant value for accurately modeling the landslide displacement patterns, despite having larger spatiotemporal baselines. Second, as the core idea of the SAR offset tracking method is the normalized cross-correlation (NCC) calculation [19], a regular window size is exploited to calculate the NCC coefficient between two image patches and determine the maximum correlation in most previous studies (e.g., refs. [8,18]). Yet, the estimated offsets may be biased and even vary randomly when the samples in two image patches are not homogenous [20,21]. In other words, the accuracy of the estimated landslide displacement can be affected by the fixed window size in the mountainous areas. Thus, the adaptive selection of the window size is of great significance in improving the accuracy of the SAR offset tracking-retrieved displacements. Third, in retrieving the long-term displacement time series of slow-velocity landslides over a decade, offset pairs with larger temporal baselines and even from cross-platform SAR observations (e.g., ALOS/PALSAR-1 and ALOS/PALSAR-2 images) must be included. In this case, the outliers caused by low correlations will inevitably appear in the estimated offset measurements. However, most state-of-the-art time series SAR offset tracking methods [2,18,22,23] can hardly deal with this problem.

Thus, identifying the optimal selection of offset pairs, as well as the best design of the geometry of the displacement inversion network, is important for time series inversion. A network with less redundancy of offset pairs can increase the uncertainty in the estimated displacement parameters [24,25]. Related to this, two different strategies for the generation and selection of offset pairs have been proposed and applied in previous studies [2,18,26]. First, offset pairs are created using a small baseline subset strategy [18,26]. Although the pairs with small spatiotemporal baselines can maintain a higher correlation, it may lead to an error accumulation in the displacement time series, particularly in slow-moving landslides where insufficient displacement exists [2,27]. Thus, balancing the spatiotemporal baselines is essential and should depend on the landslide displacement magnitude [27]. The second option is to combine offset pairs using a strategy of a small spatial baseline and a large temporal baseline [2]. However, such a strategy has a very

limited application because of SAR images acquired from previous satellites, such as ALOS/PALSAR-1. More importantly, higher degrees of redundancy were not exploited in the two strategies mentioned above when estimating the displacements. As mentioned previously, the optimal selection of offset pairs and the optimal design of the geometry of the displacement inversion network are critical in ensuring the accuracy and reliability of the estimated displacements [27], in which the three criteria of precision, reliability, and computational cost should be considered. Related to this, the more mature optimal design of the network in the geodesy field [28] can provide great inspiration for the offset tracking community.

Furthermore, three-dimensional (3D) deformation fields can provide particular clues for understanding the type, failure mode, and subsurface sliding geometry of active landslides [22,29]. The 2D displacement field of the actively moving part of a landslide can be estimated by the SAR offset tracking method using single-orbit SAR data, thus making it possible to invert 3D displacements using SAR images from two or more observations with diverse imaging geometries [2,30]. However, multi-orbit satellite SAR observations are usually difficult to satisfy in most areas on Earth [11]. Thus, another alternative solution for retrieving 3D deformation is to add *a priori* information of landslide movement to reduce the degrees of freedom [30], when only a single-orbit SAR dataset is available. In the case of landslides, an acceptable assumption is that landslides move parallel to their ground surface; thus, by adding a parallel displacement constraint to SAR offset measurements, the 3D displacements can be estimated. The feasibility and accuracy of this approach have been demonstrated and assessed by studies on landslides and glaciers using ascending and descending InSAR measurements [31,32]. Notably, the estimated 3D displacements from this approach may be biased in the case of errors in the external digital elevation model (DEM). Thus, to address the bias caused by inaccurate DEMs, a robust estimation method for 3D landslide displacements should be explored.

Herein, we propose an improved cross-platform SAR image offset tracking approach for long-term monitoring 2D and 3D landslide displacements over a decade. This algorithm has the ability to monitor landslides that are placed on the rugged mountain areas using SAR images both from an identical platform and a cross-platform. To this end, with the goals of increasing the cross-correlation values between the SAR images with large spatiotemporal baselines and improving the precision of the offset measurements, we improved the traditional SAR offset tracking workflow by adding “ortho-rectification” operation before cross-correlation computation and adopting an adaptive matching window when conducting cross-correlation calculation. The pixel misalignments resulting from the topography relief can be

compensated by the “ortho-rectification” operation, thus allowing for the precise co-registering of the SAR images. Then, we developed a new strategy for combining offset pairs and optimally designing the geometry of the displacement inversion network based on the theory of optimization and design of the geodetic network. Next, the robust estimation algorithms, namely, M-estimator and total least squares (TLS) estimator, were introduced to restrain the outliers and deal with the inaccurate DEM in 2D and 3D displacement time series inversion of landslides. We applied the developed procedure to monitor the nearly 13-year 2D and 3D displacements of the Laojingbian landslide located in the Wudongde Reservoir Area, Jinsha River, China, using SAR images acquired from cross-platform ALOS/PALSAR-1 and ALOS/PALSAR-2 sensors between August 2007 and May 2020. In particular, we performed an early warning and displacement forecasting of the landslide by fusing the estimated 3D long-term displacement time series and the unidimensional constitutive models of rocks. Then, from such information, we inferred the possible impacting factor for landslide activity using the residuals of modeled displacements from unidimensional constitutive models of rocks.

2 Methodology

The components of the proposed workflow are shown in Figure 1, where the light orange rectangles indicate the focus and improvements in this study, and the light blue rectangles are the standard procedures in SAR offset tracking computation. The proposed procedure focuses on the three shortcomings of traditional SAR offset tracking methods in the time series displacement mapping of slow-velocity landslides, especially in complex areas, such as rugged mountain areas, steep terrains, and non-homogenous targets. For the first solution, the ortho-rectification of the SAR images was added to remove topographic relief effects and achieve accurate co-registration of SAR images from identical and cross platforms. Second, adaptively varying windows were introduced into the cross-correlation computation to avoid the bias caused by non-homogenous samples in two image patches, thus improving the accuracy of the azimuth and slant-range offset measurements, particularly for offset pairs with longer spatial baselines. Third, high-quality offset pairs were optimally selected to design the network of displacement inversion based on the measurement uncertainties and the theory of optimization and design of geodetic networks. Fourth, the mathematical equation of 2D displacement rates and time series inversion was established using the designed network, into which the M-estimator [33] was introduced to restrain the outliers caused by low correlation. Next, the 3D displacement inversion based on the surface-parallel flow model [31] and the estimated 2D displacements were fol-

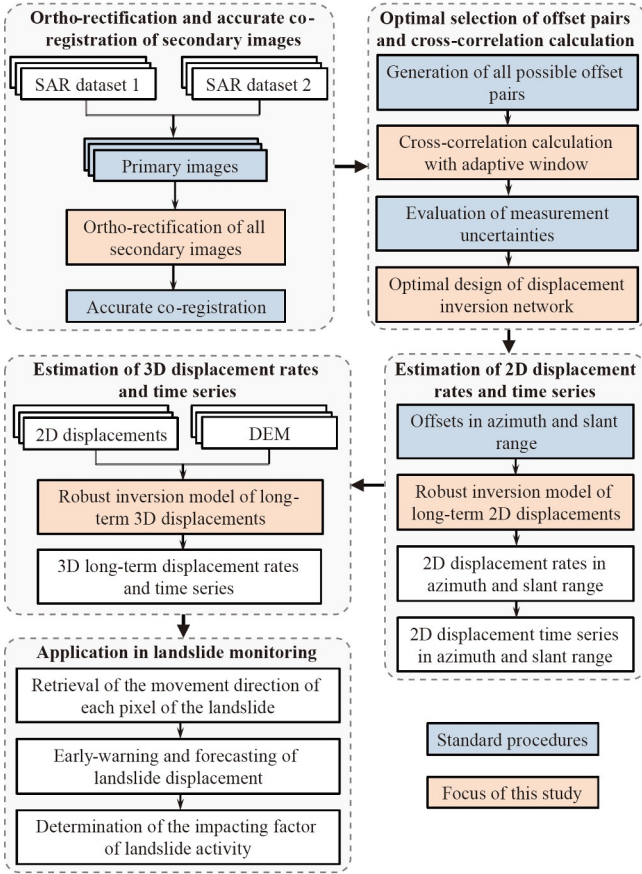


Figure 1 Workflow for the improved cross-platform SAR image offset tracking approach for monitoring the long-term 2D and 3D landslide displacements. The main focus and contributions of this study are highlighted in light orange and the standard procedures in light blue.

lowed. The TLS algorithm was applied to estimate the 3D displacement rates and time series, given that random errors exist not only in the observations but also in the coefficient matrix (caused by inaccurate DEM). Finally, we retrieved the sliding direction of each pixel of the landslide using the derived horizontal displacement rates, conducted an early warning of landslides using 3D long-term displacement time series, and further forecasted the temporal evolution of landslide displacement in the following five years based on the unidimensional constitutive models of rocks. The different steps of the procedure are described in detail in the following subsections.

2.1 Ortho-rectification and accurate co-registration of SAR images

A stringent prerequisite in SAR offset tracking estimation is the accurate co-registration between primary and secondary images, because the accuracy of SAR offset tracking-derived displacement is subject to the co-registration accuracy. Previous studies [17,34,35] have demonstrated that topographic

relief can lead to pixel misalignments in SAR images, which can significantly decrease the precise registration of SAR images. For offset pairs with a smaller spatial baseline and moderate topography, the offset errors arising from topographic relief can be neglected [2,18,35]. However, such potential errors must be considered for offset pairs with longer spatial baseline and rugged terrains [23,34,35], particularly for offset pairs from the cross-platform (e.g., ALOS/PALSAR-1 and ALOS/PALSAR-2). In the current work, a pre-processing step, namely “ortho-rectification,” based on the SAR imaging geometry and external DEM [23,35], is conducted to remove the topographic relief effects. Then, the primary and secondary images are accurately co-registered based on the ortho-rectified SAR images. The rationale and procedures are described as follows [23,34,35].

(i) The optimal primary images within SAR images from an identical platform and cross-platform were determined based on Doppler central frequency variations and spatio-temporal baselines. Then, based on the SAR imaging geometry and the external DEM, the direct functions that record the location of each pixel in the primary image to a corresponding pixel position in the secondary image were established.

(ii) The established functions were refined to deal with the bias caused by errors in the orbital state vectors of the SAR images and the external DEM.

(iii) The rectified SAR images were further obtained by resampling all the secondary SAR images to the frame of the primary images based on the refined functions.

To demonstrate the effects of topographic relief and the necessity of the ortho-rectification operation, four exemplary offset pairs from an identical platform (ALOS/PALSAR-1 and ALOS/PALSAR-1) and the cross-platform (ALOS/PALSAR-1 and ALOS/PALSAR-2) with extremely large spatial baselines were selected to illustrate the co-registration accuracy with and without ortho-rectification, as shown in Table 1. In the table, we can see that the results with ortho-rectification operation show improved co-registration accuracy and that the accuracies in the azimuth and range directions are all better than 1/10 pixels, even when the spatial baseline is longer than 100 km.

2.2 Cross-correlation computation with adaptively varying windows

The accuracy of the SAR offset tracking estimation can be expressed as [36]

$$\sigma_{r,a} = \sqrt{\frac{3}{2N}} \cdot \frac{\sqrt{1-\gamma^2}}{\pi\gamma}, \quad (1)$$

where $\sigma_{r,a}$ is the standard deviation of the offset tracking estimation, N indicates the number of samples in an image patch, and γ is the cross-correlation value of the image patch.

Table 1 Co-registration accuracies of primary and secondary images with and without ortho-rectification^{a)}

Offset pairs	Image type	TB (d)	SB (m)	Without ($Rg \times Az$) (pixel)	With ($Rg \times Az$) (pixel)
20080829-20110307	A1, A1	920	4641	0.18×0.06	0.03×0.05
20081014-20110307	A1, A1	874	3714	0.13×0.05	0.02×0.05
20101205-20141205	A1, A2	1461	109669	0.66×0.32	0.07×0.09
20110307-20150925	A1, A2	1663	108784	0.32×0.19	0.07×0.04

a) A1 and A2 represent ALOS/PALSAR-1 and ALOS/PALSAR-2 images, respectively; TB and SB represent temporal and spatial baselines, respectively; and without and with indicate co-registration accuracy without and with ortho-rectification, respectively.

Notably, eq. (1) is derived for a homogenous image patch; that is, the features of the samples in the two image patches are nearly identical [20]. Therefore, the offset measurement may significantly vary with the size of the image patch, the oversampling factor, and the number of samples in areas with unstable features and should be relatively constant in areas with stable features [21]. The standard SAR offset tracking methods typically calculate the offsets using a single fixed window size, such as 128×128 pixels or 64×64 pixels, which are determined empirically. As a result, the estimated offsets may be largely biased for image patches with low correlations (e.g., in mountainous areas and in dense vegetation areas) and with dominant scatterers [12,21]. Thus, we employed adaptively varying windows to perform cross-correlation computation between image patches to avoid biased results in low-correlation scenarios and improve the accuracy of SAR offset tracking estimation. For a generic given pixel (i), a set of sub-pixel offsets (i.e., $of_{i1}, of_{i2}, of_{i3}, of_{i4}, \dots, of_{iN}$) was estimated by changing the oversampling factor (e.g., from 2 to 8) and the size of the image patches (e.g., from 8×8 to 256×256). Considering computational efficiency, an optimally fixed oversampling factor was determined in practice. Then, each element in the set of the estimated offset was arranged according to the magnitude of the offset values, and the median value was selected as the final offset for the given pixel (i), thus effectively restraining the outliers.

2.3 Estimation of the measurement uncertainty

Estimating the measurement uncertainty over a stable area would be useful in assessing the accuracy of the obtained displacements in the case of the paucity of *in situ* measurements [27]. The mean value (MEV) and standard deviation (STD) are commonly used to estimate uncertainties by researchers [37,38]. The MEV represents a general shift in the estimated displacement (i.e., systematic uncertainty), whereas the STD indicates random variations (i.e., stochastic uncertainty). Based on the law of error propagation, we calculated the total measurement uncertainty as a function of the MEV and STD of the displacement over landslide-free areas. The mean square error (MSE) of the displacement was

estimated using the following equation:

$$MSE = \sqrt{MEV^2 + STD^2}. \quad (2)$$

2.4 Optimal selection strategy of offset pairs

We constructed the optimal selection strategy of offset pairs based on the measurement uncertainties and the theory of optimization and design of the geodetic network, in which three criteria (precision, reliability, and computational cost) were considered. Consequently, our method was oriented toward selecting high-quality pairs to reduce time costs and errors, which mainly consisted of three steps, as described below.

(i) All possible offset pairs were created by merely considering the temporal baseline, regardless of the spatial baseline, thus forming highly redundant observations. The minimum temporal baseline threshold ($B_{T_{thres}}$) with units of days is defined as follows:

$$B_{T_{thres}} = \frac{PS \cdot \delta_{off}}{def_rate}, \quad (3)$$

where PS is the pixel size, δ_{off} is the measurement accuracy ($\sim 1/10$ – $1/30$ pixels) of the offset tracking method, and def_rate is the daily displacement rate of the landslide.

(ii) After calculating the offsets in the azimuth and slant-range directions of all generated pairs, the pairs with high quality were selected for further processing, in which the pairs with larger measurement uncertainty (MSE) were discarded and those with smaller MSEs were retained.

(iii) The configuration of the selected pairs (i.e., displacement inversion network) was further optimized using the redundancy numbers (i.e., r-numbers) of the observations from the geodesy community [39]. In geodesy communities, r-numbers are generally used as a measure to optimally design a geodetic network with high reliability [28]. Therefore, to ensure the high reliability of the displacement inversion network, we exploited the r-numbers to further optimize the selected offset pairs. The r-numbers are the diagonal elements of the matrix \mathbf{R} , which can be mathematically written as [39]

$$\mathbf{R} = \mathbf{I} - \mathbf{A}(\mathbf{A}^T \mathbf{P} \mathbf{A})^{-1} \mathbf{A}^T \mathbf{P}, \quad (4)$$

where \mathbf{I} indicates the identity matrix, \mathbf{A} is the design matrix of the displacement inversion network, and \mathbf{P} is the weight matrix associated with the uncertainty of each observation, that is, $\mathbf{P}=\text{diag}(1/\text{MSE}_1^2, \dots, \text{MSE}_M^2)$. A smaller r -number corresponds to an unacceptable offset pair and should be removed when calculating the 2D and 3D displacements. In this study, a total of 66 offset pairs were finally selected to estimate the displacement time series, among which 27 were from the ALOS/PALSAR-1 dataset, 7 from the ALOS/PALSAR-1 and ALOS/PALSAR-2 datasets, and 32 from the ALOS/PALSAR-2 dataset. The spatiotemporal baseline configurations of the selected offset pairs are presented in Figure 2. As can be seen, the largest spatial baselines of the

ALOS/PALSAR-1 and ALOS/PALSAR-2 offset pairs reached 2843 and 250 m, respectively, which are even larger than 108.5 km between the ALOS/PALSAR-1 and ALOS/PALSAR-2 images.

2.5 Estimation of 2D displacement rates and time series

After performing the 2D offset calculations of all selected offset pairs, the observational equation of the 2D displacement inversion can be mathematically written as follows:

$$\mathbf{A}\bar{\mathbf{X}} + \mathbf{V} = \mathbf{L}, \quad (5)$$

where

$$\mathbf{A} = \begin{pmatrix} \text{ALOS}_1 \begin{cases} t_2 - t_1 & t_3 - t_2 & 0 & \dots & 0 & 0 & 0 & \dots & 0 & 0 & 0 \\ 0 & t_3 - t_2 & t_4 - t_3 & \dots & 0 & 0 & 0 & \dots & 0 & 0 & 0 \\ \vdots & \vdots & \vdots & \dots & \vdots & \vdots & \vdots & \dots & \vdots & \vdots & \vdots \end{cases} \\ \text{ALOS}_{1,2} \begin{cases} 0 & 0 & 0 & \dots & t_i - t_{i-1} & t_{i+1} - t_i & 0 & \dots & 0 & 0 & 0 \\ 0 & 0 & 0 & \dots & 0 & t_{i+1} - t_i & t_{i+2} - t_{i+1} & \dots & 0 & 0 & 0 \\ \vdots & \vdots & \vdots & \dots & \vdots & \vdots & \vdots & \dots & \vdots & \vdots & \vdots \end{cases} \\ \text{ALOS}_2 \begin{cases} \vdots & \vdots & \vdots & \dots & \vdots & \vdots & \vdots & \dots & \vdots & \vdots & \vdots \\ 0 & 0 & 0 & \dots & 0 & 0 & 0 & \dots & t_{n-1} - t_{n-2} & t_n - t_{n-1} & 0 \\ 0 & 0 & 0 & \dots & 0 & 0 & 0 & \dots & 0 & t_n - t_{n-1} & t_{n+1} - t_n \end{cases} \end{pmatrix}$$

is the design matrix;

$$\bar{\mathbf{X}} = \begin{pmatrix} \text{ALOS}_1 \begin{cases} x_1 \\ x_2 \\ \vdots \end{cases} \\ \text{ALOS}_{1,2} \begin{cases} x_{i-1} \\ x_i \end{cases} \\ \text{ALOS}_2 \begin{cases} \vdots \\ x_{n-1} \\ x_n \end{cases} \end{pmatrix}$$

is the unknown displacement vector;

$$\mathbf{L} = \begin{pmatrix} \text{ALOS}_1 \begin{cases} l_1 \\ l_2 \\ \vdots \end{cases} \\ \text{ALOS}_{1,2} \begin{cases} l_{i-1} \\ l_i \end{cases} \\ \text{ALOS}_2 \begin{cases} \vdots \\ l_{n-1} \\ l_n \end{cases} \end{pmatrix}$$

is the observation matrix—that is, the estimated offsets in the azimuth or slant-range direction; and \mathbf{V} is the residual of the observation matrix. To estimate long-term 2D landslide displacements, the observations presented in eq. (5) are not only from an identical SAR platform (i.e., ALOS/PALSAR-1 or ALOS/PALSAR-2) but also from the cross-platform (i.e.,

ALOS/PALSAR-1 and ALOS/PALSAR-2).

In general, the solution of the displacement rate vector \mathbf{X} can be obtained using the least square criterion ($V^T P V = \text{min}$) as follows [2]:

$$\bar{\mathbf{X}} = (\mathbf{A}^T \mathbf{P} \mathbf{A})^{-1} \mathbf{A}^T \mathbf{P} \mathbf{L}. \quad (6)$$

Observations from offset pairs with larger temporal baselines were considered to generate the long-term displacement time series and retrieve the movement of slow-velocity landslides. However, this may inevitably raise outliers in offset tracking observations. As the LS method can be easily affected by outliers in observations, we introduced a robust estimation [33] to effectively restrain the outliers in observations. Owing to its high computational efficiency and better performance in restraining outliers, the M-estimator [33] was applied to robustly estimate the 2D long-term displacement rates and time series in this study. The optimal solution of $\bar{\mathbf{X}}$ can be estimated by iterative computation with variable weights:

$$\bar{\mathbf{X}}^{k+1} = (\mathbf{A}^T \bar{\mathbf{P}}^k \mathbf{A})^{-1} \mathbf{A}^T \bar{\mathbf{P}}^k \mathbf{L}, \quad (7)$$

where $\bar{\mathbf{P}}$ is the equivalent weight matrix of \mathbf{P} , which can be constructed by applying the Huber [33] function, as presented in eq. (8). The iteration is terminated when it satisfies the convergence condition of $|\bar{\mathbf{X}}^{k+1} - \bar{\mathbf{X}}^k| < \varepsilon$, where ε is the tolerance of the control iteration. Once the robust estimates of 2D displacement rates are obtained in the azimuth and slant-range directions between two time-adjacent SAR ac-

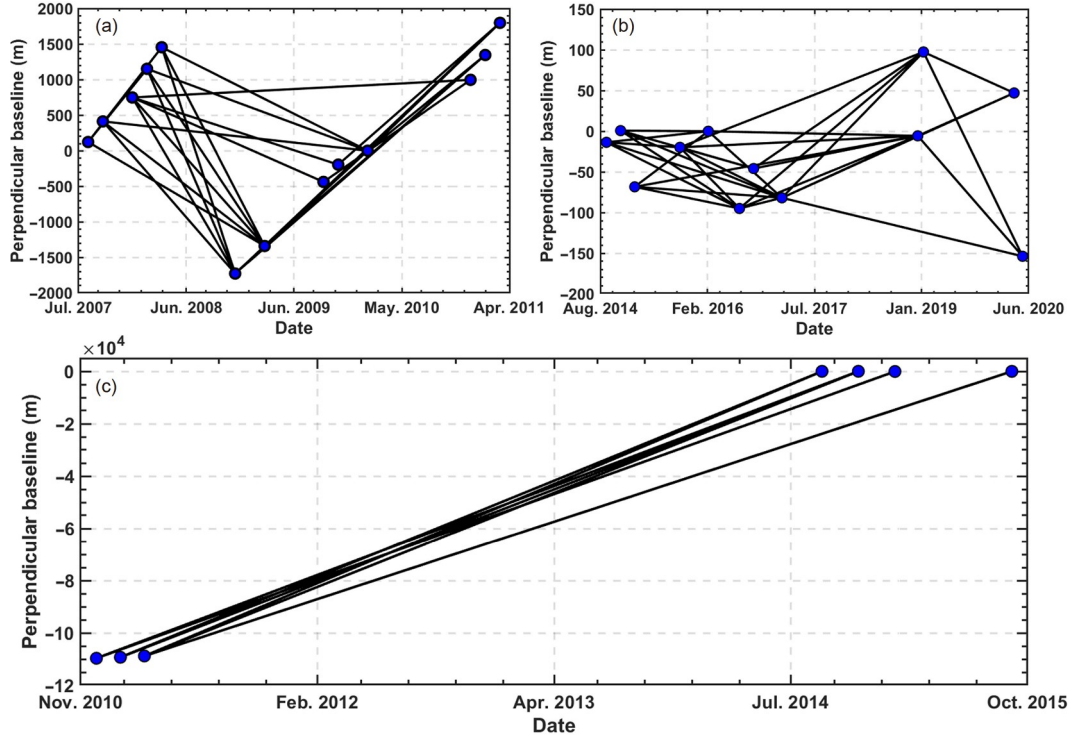


Figure 2 Spatiotemporal baseline configurations of the offset pairs selected in this study. (a) ALOS/PALSAR-1 dataset; (b) ALOS/PALSAR-2 dataset; (c) ALOS/PALSAR-1 and ALOS/PALSAR-2 datasets.

quisitions, the 2D displacement time series at each SAR acquisition can be calculated using numerical integration:

$$\bar{P}_i = \begin{cases} p_i, & |v_i| \leq 2\sigma_0, \\ p_i \frac{2\sigma_0}{|v_i|}, & |v_i| > 2\sigma_0, \end{cases} \quad (8)$$

where σ_0 is a given constant value.

2.6 Estimation of 3D displacement rates and time series

Due to the side-looking configurations of all SAR satellites, the offset tracking-derived slant-range (D_{SR}) and azimuth (D_{AZI}) displacements are the projections of the real 3D ground surface displacements in the north (D_N), east (D_E), and vertical (D_U) directions [40], as shown in eq. (9)

$$\begin{cases} D_N \cdot \sin\theta \cdot \sin\alpha - D_E \cdot \sin\theta \cdot \cos\alpha + D_U \cdot \cos\theta \\ = D_{SR} + \Delta D_{SR}, \\ D_N \cdot \cos\alpha + D_E \cdot \sin\alpha = D_{AZI} + \Delta D_{AZI}, \end{cases} \quad (9)$$

where θ and α are the incidence angle and flight direction of the SAR satellite, respectively, and ΔD_{AZI} and ΔD_{SR} are the corresponding observation errors of the azimuth and slant-range displacements, respectively. Given that eq. (9) is a rank-deficient model for estimating the 3D displacements, constraints should be introduced to stabilize the rank-deficient model. For gravity-driven landslide movement, the

constraint can be constructed in terms of the following displacement [31,32]:

$$\frac{\partial H}{\partial Y} \cdot D_N + \frac{\partial H}{\partial X} \cdot D_E - D_U = 0, \quad (10)$$

where H is the elevation of the terrain, and $\frac{\partial H}{\partial X}$ and $\frac{\partial H}{\partial Y}$ are the first derivatives in the east (X) and north (Y) directions, respectively, which can be calculated from the external DEM. Thus, the 3D displacements of the landslide can be resolved by combining eqs. (9) and (10), which are simplified into the following matrix form:

$$\widehat{\mathbf{A}}\mathbf{X} = \mathbf{L} + \Delta\mathbf{L}, \quad (11)$$

where

$$\widehat{\mathbf{A}} = \begin{bmatrix} \sin\theta\sin\alpha & -\sin\theta\cos\alpha & \cos\theta; & \cos\alpha & \sin\alpha & 0; & \frac{\partial H}{\partial Y} & \frac{\partial H}{\partial X} & -1 \end{bmatrix}$$

is the design matrix; $\mathbf{X} = [D_N \ D_E \ D_U]^T$ are the unknown 3D displacements in the north, east, and vertical directions, respectively; and $\mathbf{L} = [D_{SR} \ D_{AZI} \ 0]$ are the displacement observations in the slant-range and azimuth directions. The routine method for resolving eq. (11) is to use the LS or SVD method (e.g., ref. [41]). However, the design matrix $\widehat{\mathbf{A}}$ may contain random errors due to the uncertainty in the external DEM; therefore, eq. (11) can be rewritten as follows:

$$(\bar{\mathbf{A}} + \Delta\widehat{\mathbf{A}})\mathbf{X} = \mathbf{L} + \Delta\mathbf{L}, \quad (12)$$

where $\bar{\mathbf{A}}$ is the true matrix of $\widehat{\mathbf{A}}$, and $\Delta\widehat{\mathbf{A}}$ is a matrix of

random error. Although the LS method can deal with random errors in observations, it is unable to deal with random errors in the design matrix because eq. (12) is nonlinear. The TLS method [42], which is based on the errors-in-variables model, has been developed to address this problem. Thus, the TLS method was introduced in the current study to robustly estimate the 3D displacement rates and time series. The mean vectors and variance-covariance matrices of the error vectors can be written in the following form:

$$\begin{bmatrix} \Delta \mathbf{L} \\ \text{vec}(\Delta \mathbf{A}) \end{bmatrix} \sim N \left(\begin{bmatrix} 0 \\ 0 \end{bmatrix}, \begin{bmatrix} \sum_L & 0 \\ 0 & \sum_A \end{bmatrix} \right), \quad (13)$$

where $\text{vec}(\cdot)$ indicates the straightening transformation of the matrix, and \sum_L and \sum_A are the variance-covariance matrices of $\Delta \mathbf{L}$ and $\Delta \mathbf{A}$, respectively. Thus, eq. (12) can be rewritten as eq. (14), and the optimal estimation criterion for the TLS solution is presented in eq. (15) [42].

$$[\mathbf{A} + \Delta \mathbf{A} \quad \mathbf{L} + \Delta \mathbf{L}] \cdot \begin{bmatrix} \mathbf{X} \\ -1 \end{bmatrix} = ([\mathbf{A} \quad \mathbf{L}] + \Delta) \cdot \begin{bmatrix} \mathbf{X} \\ -1 \end{bmatrix} = 0, \quad (14)$$

$$\text{vec}(\Delta \mathbf{A})^T \cdot \text{vec}(\Delta \mathbf{A}) + (\Delta \mathbf{L})^T \cdot \Delta \mathbf{L} = \min, \quad (15)$$

The augmented matrix (\mathbf{G}) of eq. (14) can be mathematically written as follows:

$$\mathbf{G} = [\mathbf{A} \quad \mathbf{L}] = \begin{bmatrix} \mathbf{U}_1 & \mathbf{U}_2 \\ m+1 & n-(m+1) \end{bmatrix} \cdot \begin{bmatrix} \mathbf{S} \\ 0 \end{bmatrix} \cdot \mathbf{V}^T, \quad (16)$$

where $\mathbf{U} = [\mathbf{U}_1 \quad \mathbf{U}_2]$ is an orthogonal matrix composed of n

eigenvectors of matrix $[\mathbf{A} \quad \mathbf{L}] \cdot [\mathbf{A} \quad \mathbf{L}]^T$, $\mathbf{V} = \begin{bmatrix} \mathbf{V}_{11} & \mathbf{V}_{12} \\ \mathbf{V}_{21} & \mathbf{V}_{22} \end{bmatrix}_m$ is an

orthogonal matrix composed of $m+1$ eigenvectors of matrix

$\begin{bmatrix} \mathbf{A}^T \mathbf{A} & \mathbf{A}^T \mathbf{L} \\ \mathbf{L}^T \mathbf{A} & \mathbf{L}^T \mathbf{L} \end{bmatrix}$, and $\mathbf{S} = \text{diag}(\sigma_1, \sigma_2, \dots, \sigma_{m+1})$ is the singular

value of the augmented matrix (\mathbf{G}). The TLS solution of the 3D displacement vector \mathbf{X} can be obtained using the matrix approximation theory of Eckart-Young-Mirsky [43,44], which is formulated as follows:

$$\hat{\mathbf{X}} = -\mathbf{V}_{12} \cdot \mathbf{V}_{22}^{-1}. \quad (17)$$

3 Study area and datasets

3.1 Study area

The study area is located in the Wudongde Reservoir Area in the lower reaches of the Jinsha River in Yunnan Province, China (Figure 3). The reservoir area is situated on the southeast edge of the Qinghai-Tibet Plateau (Figure 3(b)) and constitutes a transition zone between the Yunnan-Guizhou Plateau and the Sichuan Basin, thus producing a special geological setting, including deep and narrow valleys and high mountains (Figure 3(a)) [45,46]. The study area is

one of the strongest tectonically active and seismically prone areas in China. Moreover, it belongs to the subtropical monsoon climate zone, characterized by concentrated rainfall, strong solar radiation, and high daily temperature difference [46], thereby causing strong weathering of the slope materials. The annual average precipitation, ranging from 600–800 mm, is mainly concentrated from June to October each year. This area is strongly susceptible to landslides due to the combined effects of gravity, physical weathering, seismic activities, and heavy rainfall [46,47].

Furthermore, the impoundment and discharge of reservoirs result in adverse changes in the artificial and geological environments, which may increase the risk of new landslide development and ancient landslide reactivation [3,45]. Accordingly, the SAR-based, long-term time series displacement monitoring of large-gradient landslides is critical for hazard forecasting. Figure 3(c) shows an optical remote sensing image of the Laojingbian landslide acquired in January 2020 from Google Earth, and evidence shows the development of serious disruptions and tensile cracks on the slope surface. The altitudes in the foot and head sections of the landslide are approximately 2130 and 3100 m a.s.l., respectively, with a height difference of 970 m. There are two faults that intersect with each other in the trailing section of the slope (see the yellow lines in Figure 3(c)).

3.2 SAR datasets and ancillary data

We collected two stacks of SAR datasets from ascending ALOS/PALSAR-1 and ALOS/PALSAR-2 sensors covering the entire study area, including 14 scenes of ALOS/PALSAR-1 images acquired between August 2007 and March 2011 and 12 ALOS/PALSAR-2 images acquired between September 2014 and May 2020. There is a time gap of more than three years between the last scene of the ALOS/PALSAR-1 stack and the first scene of the ALOS/PALSAR-2 imagery. The study site is an east-facing slope with steep terrain (Figure 3(a) and (c)). Thus, to alleviate the geometrical distortions and maximize visibility, ascending track SAR images were selected. The coverage of the SAR images is shown in Figure 3(a), and the basic SAR parameters are listed in Table 2. Moreover, an ALOS global digital surface model (AW3D30 DSM) data with one arc-second (~30 m) resolution was used to compute the direction derivatives of the terrain and remove the systematic offset errors caused by topographic relief.

4 Performance analysis of the proposed approach

The performance of the proposed approach was assessed and validated by mapping the displacements of the Laojingbian

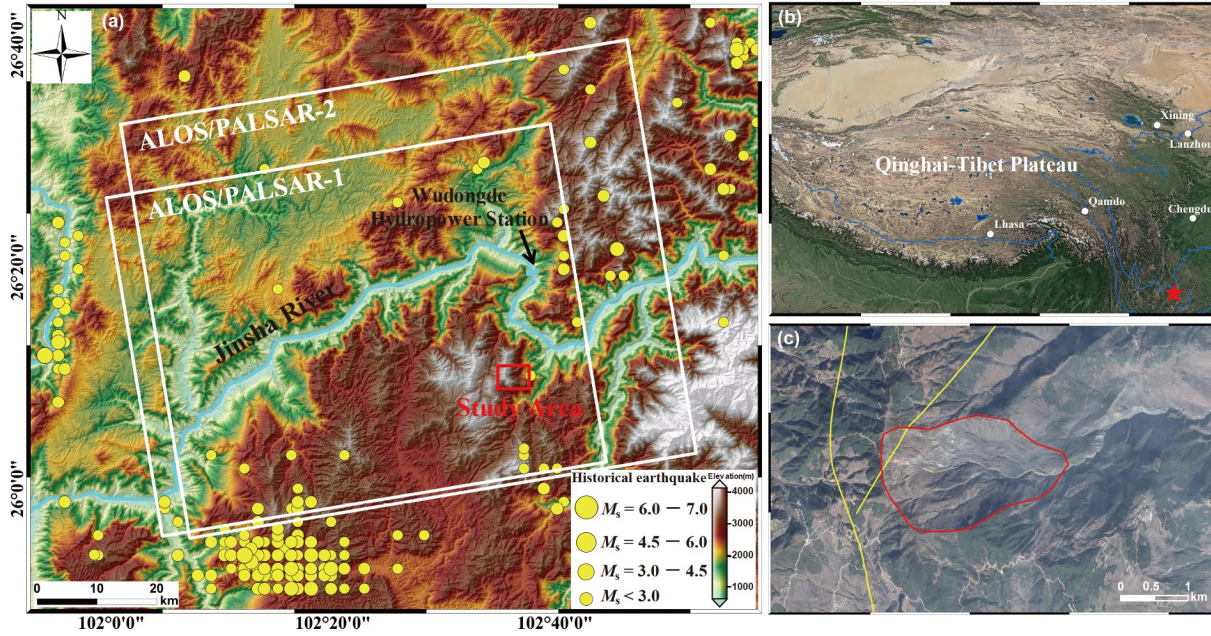


Figure 3 (a) Topography of the study area and coverage of SAR datasets, in which the study area is shown as a red rectangle and the coverages of the SAR datasets are illustrated by the white rectangles; (b) geographic location of the Laojingbian landslide (see the red star) in the Qinghai-Tibet Plateau, China; (c) optical remote sensing image of the Laojingbian landslide acquired in January 2020 from Google Earth, where the red polygon indicates the landslide boundary and the yellow lines delineate the existing faults.

Table 2 Basic parameters of the ALOS/PALSAR-1 and ALOS/PALSAR-2 images

Satellites	ALOS/PALSAR-1	ALOS/PALSAR-2
Flight direction	Ascending	Ascending
Incidence angle (°)	38.744	31.405
Azimuth (°)	-10.39	-10.71
Pixel spacing ($R_g \times A_z$)	4.68 m \times 3.17 m	4.29 m \times 3.25 m
Number of images	14	12
Number of offset pairs	27	32
Temporal coverage	August 27, 2007–March 7, 2011	September 26, 2014–May 15, 2020

landslide (Figure 3), using the cross-platform ALOS/PALSAR-1 and ALOS/PALSAR-2 SAR observations between August 2007 and May 2020. First, we assessed the performance of the proposed methods in terms of offset pairs with larger spatiotemporal baselines and from cross-platform ALOS/PALSAR-1 and ALOS/PALSAR-2 images by comparing the results derived from the proposed and traditional methods. Second, the performance of our 2D displacement inversion method that restrains the outliers was assessed through a simulated experiment.

4.1 Performance for larger spatiotemporal baseline pairs

To validate the performance of our proposed method by using three offset pairs from ALOS/PALSAR-1 images with larger spatiotemporal baselines, we compared the results

obtained from the traditional method and the proposed method qualitatively and quantitatively, as there were no GNSS data or other *in situ* measurements. Figure 4 shows the displacements in the slant-range direction, which we calculated using the traditional (left) and the proposed (right) methods. The statistical histograms of the displacements in the landslide-free areas are presented in Figure S1. The first pair (Figures 4(a), (b) and S1(a)) was generated using the ALOS/PALSAR-1 SAR images acquired on August 29, 2008, and on January 20, 2011, and had spatial and temporal baselines of 4189 m and 874 d, respectively. The second pair (Figures 4(c), (d) and S1(b)) was generated using the ALOS/PALSAR-1 images acquired on August 29, 2008, and on March 7, 2011, and had spatial and temporal baselines were 4641 m and 920 d, respectively. The third pair (Figures 4(e), (f) and S1(c)) was generated using the ALOS/PALSAR-1 images acquired on October 14, 2008, and on March 7, 2011,

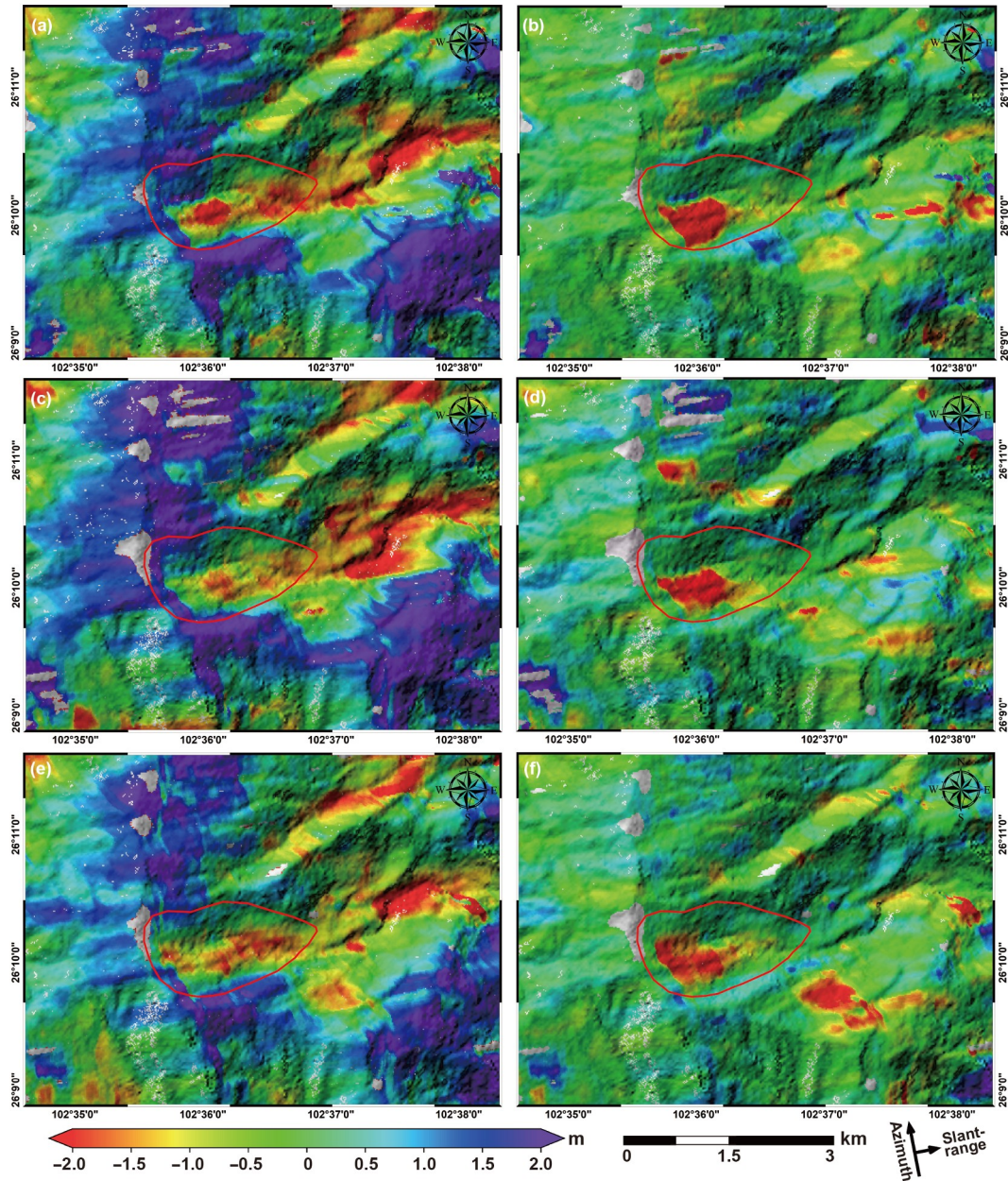


Figure 4 Comparison of the results from the ALOS/PALSAR-1 images calculated with the traditional (left) and the proposed (right) methods, respectively. The red contour delineates the landslide boundary. Slant-range displacements: (a), (b) from August 29, 2008, to January 20, 2011; (c), (d) from August 29, 2008, to March 7, 2011; (e), (f) from October 14, 2008, to March 7, 2011.

and had spatial and temporal baselines of 3714 m and 874 d, respectively. From a visual inspection of the estimated displacements, we can see from Figure 4(a), (c), and (e) that the displacement fields derived from the traditional method are severely contaminated by the systematic errors resulting from the topographic relief, particularly for areas with high altitude. In contrast, fewer systematic errors occurred in Figure 4(b), (d), and (f), which were derived from the proposed method. Moreover, it can be observed from Figure S1 that the displacement histograms derived from the proposed

method exhibited an approximately Gaussian distribution. In contrast, the ones derived from the traditional method showed a Rayleigh-like shape. This indicates that the measurements from the traditional method contain severe displacement errors and are biased [48].

To quantitatively assess the performance of the proposed approach over the traditional method, the landslide-free regions of each pair were selected to calculate the measurement uncertainties based on the rationale described in Sect. 3.3, including the MEV, STD, and MSE of the displace-

ments. Table 3 compares the uncertainties between the results estimated using the traditional and proposed methods. As shown in the table, the MEV, STD, and MSE of the displacement results estimated from the improved method are much smaller than those estimated from the proposed method, and the total uncertainties (σ) of the three pairs estimated from the improved method were all within 1 m. Furthermore, for each pair, we calculated the reduction in uncertainty in the results estimated from the proposed method defined by $\Delta\sigma = \frac{\sigma_t - \sigma_p}{\sigma_t}(\%)$, where σ_t and σ_p are the uncertainties of the displacement resulting from the traditional and improved methods, respectively. We can see from Table 3 that the parameter $\Delta\sigma$ reached 74%, 71%, and 72% for the three pairs, respectively, suggesting that the proposed method significantly improved the accuracy of the offset tracking measurements.

4.2 Performance for the cross-platform pairs

To validate the performance of the proposed method for cross-platform pairs, we selected three cross-platform offset pairs formed by the ALOS/PALSAR-1 and ALOS/PALSAR-2 image datasets. The first pair covers the period between December 5, 2010, and December 5, 2014, with spatial and temporal baselines of 109.7 km and 1461 d, respectively; the second one extends from January 20, 2011, to December 5, 2014, with spatial and temporal baselines of 109.3 km and 1415 d, respectively; and the third comprises the period between March 7, 2011, and September 25, 2015, with spatial and temporal baselines of 108.9 km and 1663 d, respectively. We compared the cross-platform displacements in the azimuth and slant-range directions of the Laojingbian landslide produced by the proposed and traditional methods. Figure 5 shows the 2D displacement maps that we calculated using the proposed method, whereas Figure S2 shows those generated using the traditional method. We can see from Figure S2 that the 2D landslide displacements are completely obscured by errors resulting from the topographic relief and the incidence angle difference between the ALOS/PALSAR-1 and ALOS/PALSAR-2 images. The offsets caused by errors in both the azimuth and slant-range directions reached 100 m. Thus, the traditional method fails to retrieve the landslide displacements between the cross-platform ALOS/

PALSAR-1 and ALOS/PALSAR-2 images. In comparison, the displacement maps calculated using the proposed method (see Figure 5) effectively eliminate the errors caused by topographic relief and incidence angle difference, thereby ensuring the accurate mapping of 2D landslide displacement fields.

To quantitatively validate the results, we analyzed the cross-correlation values of the selected pairs estimated using the traditional and proposed methods, with the results shown in Figure S3. As indicated in Figure S3, the pairs derived from the proposed method show improved cross-correlation, and the proportion of high cross-correlation values is clearly larger in the results obtained by the proposed method than those by the traditional method. This suggests that the proposed method has higher measurement precision.

5 Displacement results and analyses of the Laojingbian landslide

Using the cross-platform ALOS/PALSAR-1 and ALOS/PALSAR-2 images, we retrieved the long-term 2D displacement rates and time series of the Laojingbian landslide from August 2007 to May 2020 following the rationale described in Sect. 2.5, which is also discussed in Sect. 5.1. Then, we estimated the long-term 3D displacement rates and time series (discussed in Sect. 5.2), using the 2D displacements and external DEM, based on the method elaborated in Sect. 2.6. Finally, we evaluate the estimated displacement results in Sect. 5.3.

5.1 2D long-term displacement rates and time series

Figure 6 shows the 2D annual displacement rates of the Laojingbian landslide during different periods. In Figure 6(a), (c), and (e), the blue colors indicate that the pixels are moving along the flight direction of the satellites, while the blue colors in Figure 6(b), (d), and (f) indicate that the landslide is moving away from the satellites. Furthermore, as shown in Figure 6, the landslide movements were simultaneously measured in both the azimuth and slant-range directions, suggesting that the Laojingbian landslide has 3D movement characteristics. The maximum displacement rates in the azimuth direction from August 2007 to March 2011,

Table 3 Comparison of the uncertainties between the results estimated from the traditional and proposed methods^{a)}

Pairs	MEV (m)		STD (m)		MSE (m)		Reduced uncertainty (%)
	Trad.	Impr.	Trad.	Impr.	Trad.	Impr.	
20080829-20110120	1.68	0.43	2.63	0.67	3.12	0.80	74
20080829-20110307	1.76	0.47	2.66	0.79	3.19	0.92	71
20081014-20110307	1.47	0.44	2.30	0.62	2.73	0.76	72

a) Trad. and Impr. represent the results estimated using the traditional and improved methods, respectively.

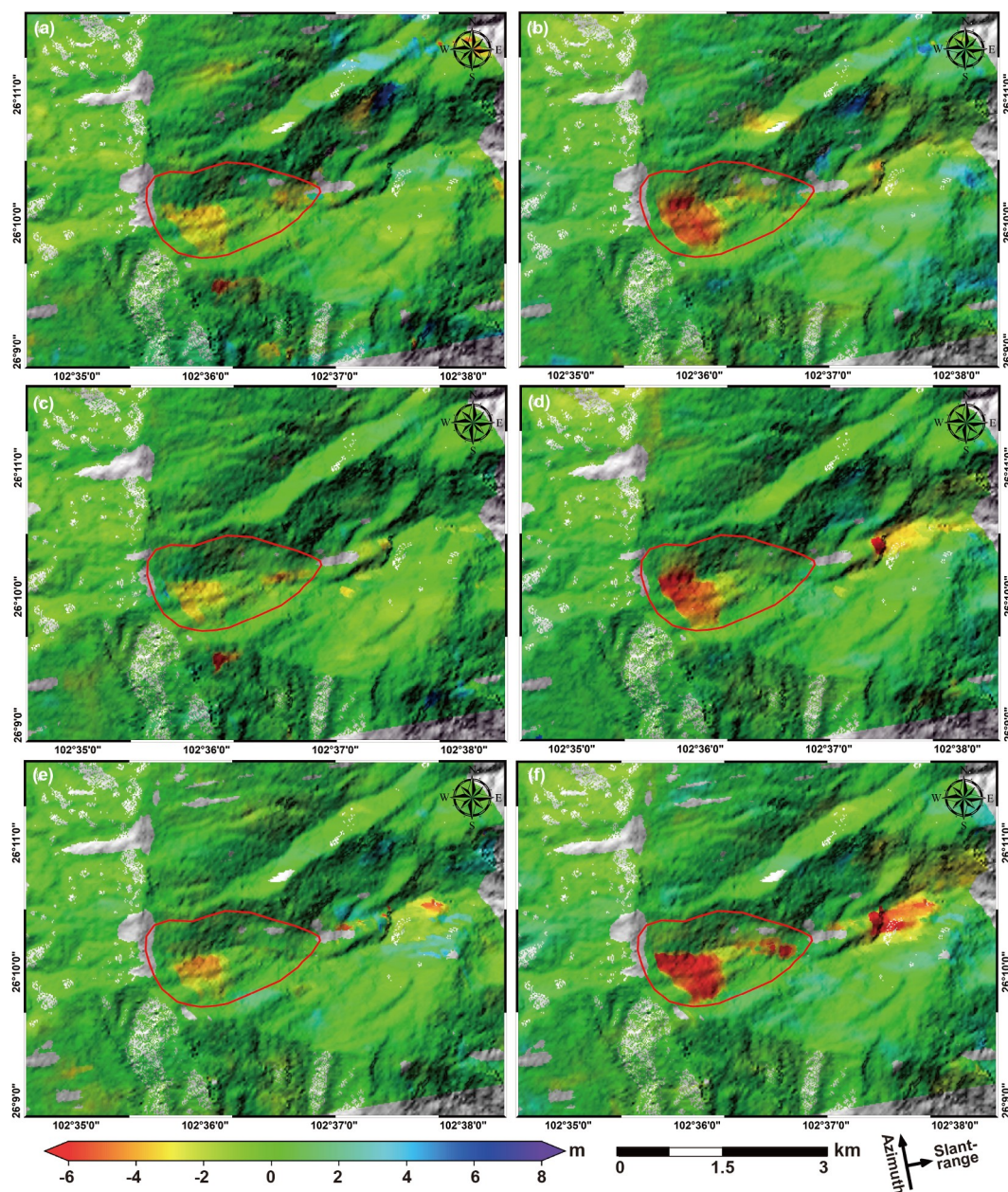


Figure 5 Cross-platform ALOS/PALSAR-1 and ALOS/PALSAR-2 displacements in the azimuth (left) and slant-range (right) directions of the Laojingbian landslide derived from the proposed method. The red lines delineate the boundary of the landslide. (a), (b) Displacements between December 5, 2010, and December 5, 2014; (c), (d) displacements between January 20, 2011, and December 5, 2014; (e), (f) displacements between March 7, 2011, and September 25, 2015.

from September 2014 to May 2020, and from August 2007 to May 2020 were -0.9 , -1.5 , and -1.0 m/year, respectively, and the corresponding displacement rates in the slant-range direction were -1.6 , -2.6 and -1.7 m/year. The results suggest that the landslide movement in the slant-range direction is approximately 1.7 times that in the azimuth direction. The average slope aspect derived from DEM indicates that the Laojingbian landslide is oriented toward the east, which is nearly perpendicular to the flight directions (approximately -10° from the north) of the ALOS/PALSAR-1 and ALOS/PALSAR-2 sensors. Thus, the observed landslide displace-

ment mainly occurred in the slant-range direction. Moreover, the 2D displacement rates of the landslide increased with time, suggesting that the landslide may have been in the accelerated displacement stage during the observational period of the ALOS/PALSAR-2 images. On the basis of the 2D displacement rates presented in Figure 6, we can observe a clear boundary of the maximum displacement regions (see the left slope). This finding demonstrates that the SAR offset tracking method has the potential to map the most active part of a landslide compared to the traditional InSAR techniques, which exhibit significant limitations in the capability to

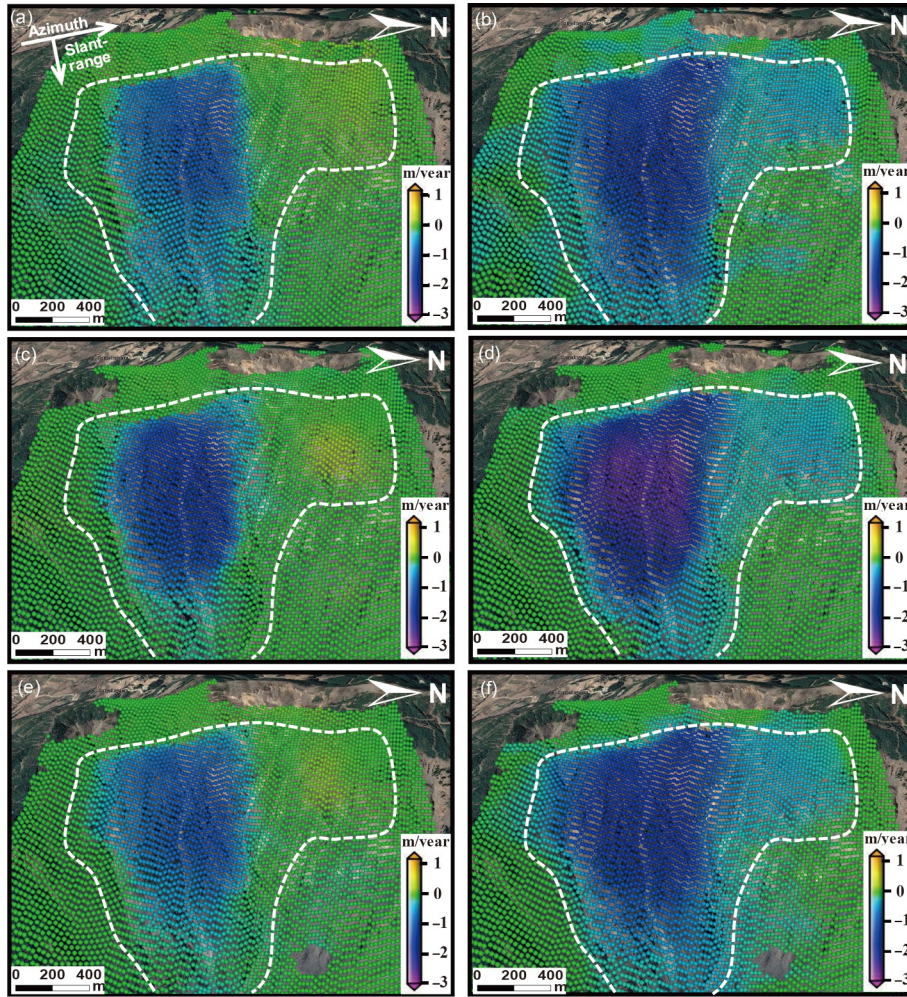


Figure 6 2D long-term displacement rates in the azimuth and slant-range directions of the Laojingbian landslide retrieved with the ALOS/PALSAR-1 and ALOS/PALSAR-2 images. The white dashed lines indicate the unstable region. (a), (b) Displacement rates in the azimuth and slant-range directions, respectively, retrieved from the ALOS/PALSAR-1 images between August 2007 and March 2011; (c), (d) displacement rates in the azimuth and slant-range directions, respectively, retrieved from the ALOS/PALSAR-2 images between September 2014 and May 2020; (e), (f) displacement rates in the azimuth and slant-range directions, respectively, retrieved from the cross-platform ALOS/PALSAR-1 and ALOS/PALSAR-2 images between August 2007 and May 2020.

measure large-gradient deformation due to the ambiguous nature of the observations [49].

Six feature points (P1–P6) located on different parts of the landslide were selected to illustrate the 2D displacement time series in the azimuth and slant-range directions. The locations of points P1–P6 are marked in Figure 12(a), where P1–P5 are located on the left slope (i.e., Block I) and P6 on the right slope (i.e., Block II). Figure 7 shows the 2D displacement time series for P1–P6 from August 2007 to May 2020, where the error bars indicate the standard deviation of the measurements. We can see that the largest cumulative displacement was observed at point P2, i.e., in the middle of Block I, the cumulative displacements in the azimuth and slant-range directions reached -13.8 and -23.8 m, respectively, within nearly 13 years; and the smallest cumulative displacements were observed at P6, i.e., in the middle of Block II, the cumulative displacements were 2.2 and -4.0 m in the azimuth and slant-range directions, respectively.

Meanwhile, larger cumulative displacements in both the azimuth and slant-range directions were also measured at P1, P3, and P5. Evidently, all points showed similar nonlinear displacement trends with varying rates and movement behaviors. The accelerated displacement signals were captured at P1, P2, P3, and P5 on September 25, 2015, which we discussed in further detail in Sect. 6.2.

5.2 3D long-term displacement monitoring

On the basis of the estimated 2D displacements in Sect. 5.1, the 3D long-term displacement rates and time series of the Laojingbian landslide were retrieved using the method described in Sect. 2.6. Figure 8 shows the 3D displacement rates in the north-south (N-S), east-west (E-W), and up-down (U-D) directions of the Laojingbian landslide from August 2007 to May 2020. The 3D displacement time series for P1–P6 marked in Figure 12(a) are presented in Figure 9. Nega-

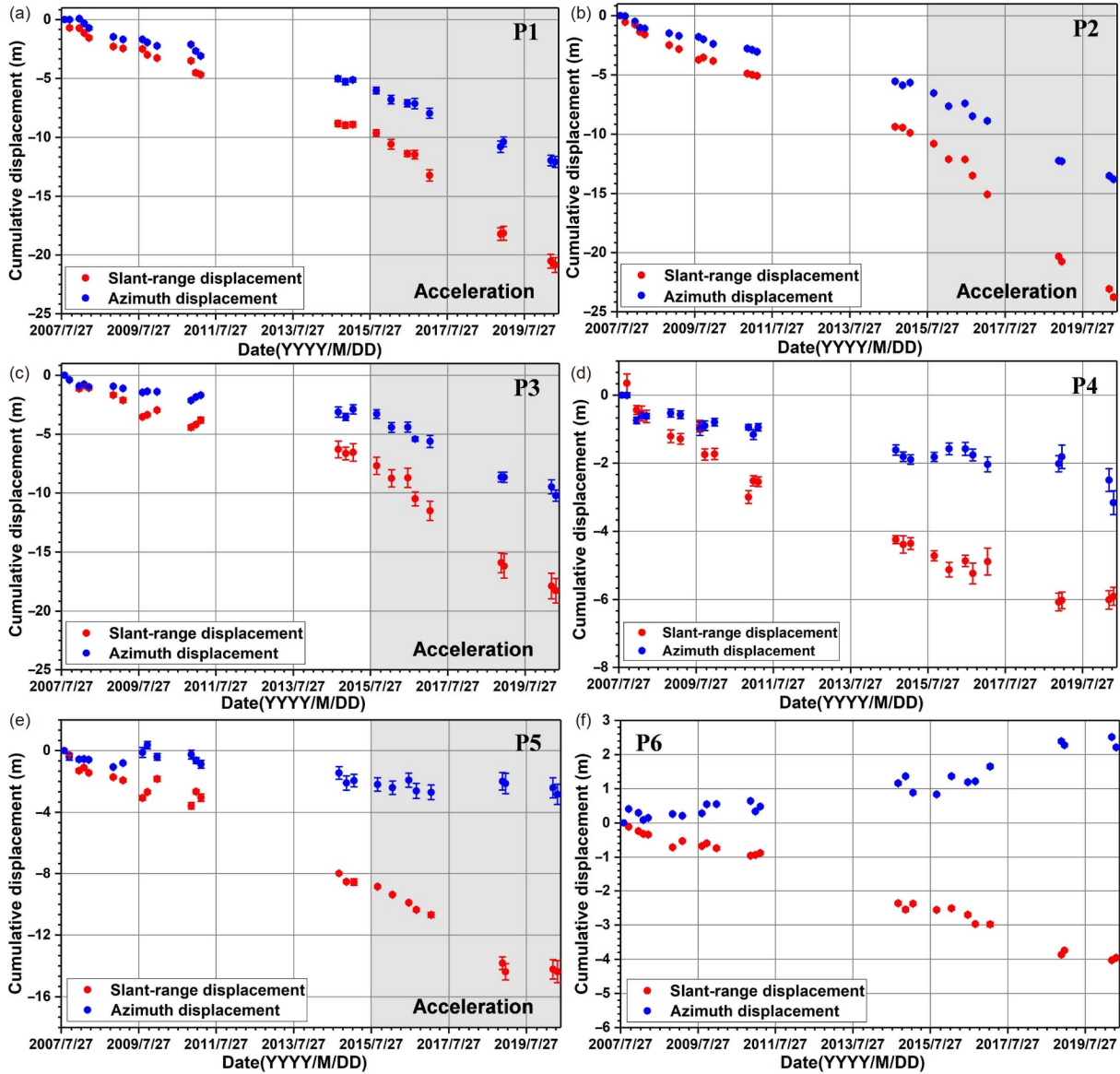


Figure 7 2D displacement time series in the azimuth and slant-range directions of the Laojingbian landslide for points P1–P6 (marked in Figure 12(a)) from August 2007 to May 2020, estimated with the cross-platform ALOS/PALSAR-1 and ALOS/PALSAR-2 images. (a) P1, (b) P2, (c) P3, (d) P4, (e) P5, and (f) P6.

tive values (blue) in the N-S displacement maps indicate northward landslide movement, negative values (blue) in the E-W displacement maps indicate eastward landslide movement, and negative values (blue colors) in the U-D displacement maps indicate downward landslide movement. The error bars in Figure 9 represent the standard deviations of the estimated 3D displacements. As shown in Figures 8 and 9, the 3D displacement fields clearly revealed the fine-scale spatiotemporal characteristics of the Laojingbian landslide, which can lead to a better understanding of the movement and failure mechanism of the slope in depth. The N-S displacement rates shown in Figure 8(a), (d), and (g) highlight the landslide with both northern movement (Block I labeled in Figure 12(a)) and southern movement (Block II

labeled in Figure 12(a)), with the maximum displacement rates of -0.6 , -0.9 , and -0.6 m/year from August 2007 to March 2011, from September 2014 to May 2020, and from August 2007 to May 2020, respectively. The E-W displacement rates shown in Figure 8(b), (e), and (h) suggest the eastward movement of the landslide, with maximum displacement rates of -2.5 , -4.3 , and -2.8 m/year from August 2007 to March 2011, from September 2014 to May 2020, and from August 2007 to May 2020, respectively. The U-D displacement rates presented in Figure 8(c), (f), and (i) indicate only downward movement of the landslide, with displacement rates of -0.7 , -1.2 , and -0.8 m/year from August 2007 to March 2011, from September 2014 to May 2020, and from August 2007 to May 2020, respectively. The results

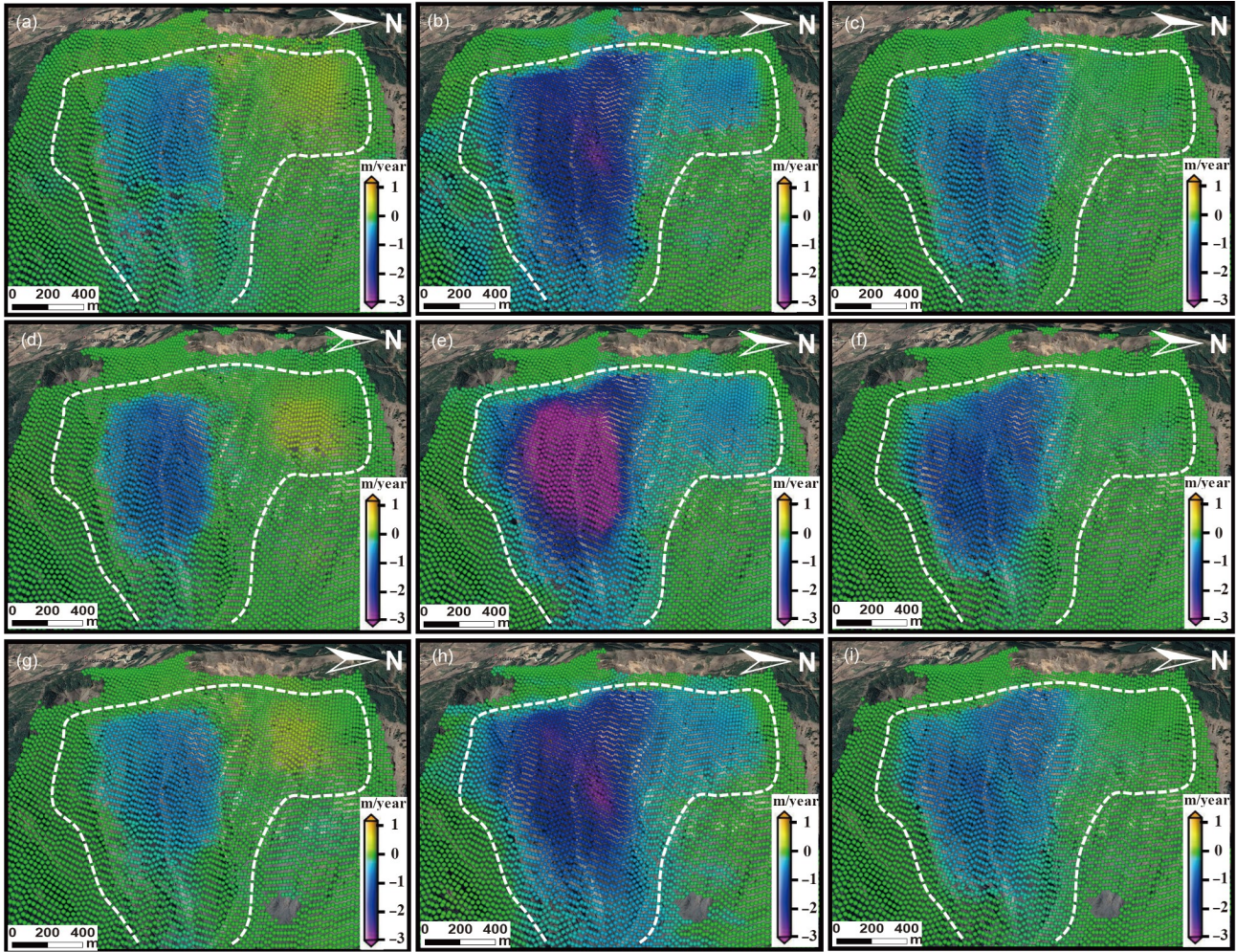


Figure 8 Estimated 3D displacement rates in the N-S, E-W, and U-D directions of the Laojingbian landslide. The white dashed lines indicate the unstable region. (a)–(c) Displacement rates in the N-S, E-W, and U-D directions, respectively, calculated with the ALOS/PALSAR-1 images from August 2007 to March 2011; (d)–(f) displacement rates in the N-S, E-W, and U-D directions, respectively, calculated with the ALOS/PALSAR-2 images from September 2014 to May 2020; (g)–(i) displacement rates in the N-S, E-W, and U-D directions, respectively, calculated with the cross-platform ALOS/PALSAR-1 and ALOS/PALSAR-2 images from August 2007 to May 2020.

revealed that the displacement in the E-W direction was much larger than those in the N-S and U-D directions, suggesting that the landslide movement was dominated by the E-W displacement. Similar to the 2D displacements in Sect. 5.1, the displacements in the three directions increased with time, and the boundary of the active part of the landslide was clearly mapped by the 3D displacements.

As seen in Figure 9, larger 3D cumulative displacements were observed at P1, P2, and P3. The cumulative displacements from August 2007 to May 2020 in the N-S, E-W, and U-D directions reached -7.3 , -26.4 , and -9.1 m, respectively for P1; -7.5 , -34.6 , and -7.9 m, respectively, for P2; and -5.4 , -26.3 , and -6.3 m, respectively, for P3. The landslide movement experienced a nonlinear evolution at these six points from August 2007 to May 2020; nevertheless, the spatial and temporal deformation patterns were inconsonant. The N-S, E-W, and U-P displacements were simultaneously observed at P1–P4 and P6, but the E-W and

U-D displacements only existed at P5. The N-S displacement at P6 was greater than the U-D displacement. However, the U-D displacements at other points were greater than or approximately equal to the N-S displacement. Similar to the 2D displacement time series presented in Figure 7, accelerated displacements were also observed at P1, P2, P3, and P5 on September 25, 2015, which we discussed in detail in Sect. 6.2.

5.3 Evaluation of the displacement results

Previous studies [27,37] have demonstrated that measurement uncertainty (MEV, STD, or MSE) can be used to evaluate the estimated displacement results. Thus, given the lack of ground-based measurements of displacements, we exploited the MSE of the displacement in landslide-free areas as an indicator to evaluate the displacement results derived from the proposed method. The MSE was calculated

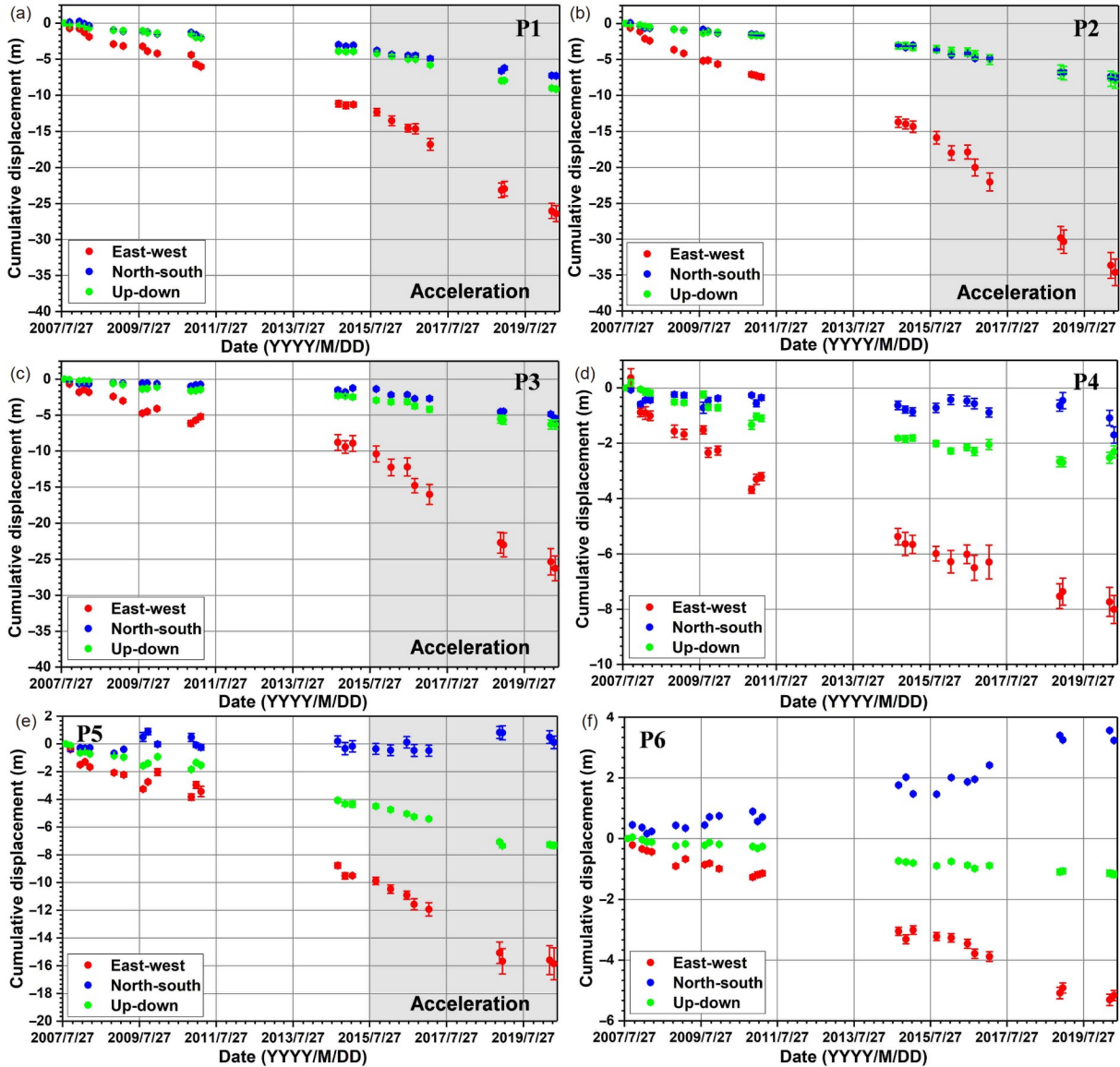


Figure 9 Estimated 3D displacement time series of the Laojingbian landslide for P1–P6 (marked in Figure 12(a)) from August 2007 to May 2020, retrieved with cross-platform ALOS/PALSAR-1 and ALOS/PALSAR-2 images. (a) P1, (b) P2, (c) P3, (d) P4, (e) P5, and (f) P6.

using eq. (2). First, we evaluated the uncertainties (i.e., MEV, STD, and MSE) of the 2D displacement rates estimated from the proposed method between August 2007 and May 2020, as shown in Figure 10. As indicated in Figure 10, the distributions of the 2D displacement rates in landslide-free areas were approximately Gaussian and did not have a Rayleigh-like shape. The MEV and STD of the 2D displacement rates were both below 0.1 m/year, while the MSE in both azimuth and slant-range directions were less than 0.15 m/year. This evidence suggests that the estimated displacement rates are unbiased measurements, as illustrated in ref. [48].

We also evaluated the MSE of the 2D displacement time series in landslide-free areas, derived from the ALOS/PALSAR-1 images, between August 2007 and March 2011.

Figure 11 shows the comparisons between the levels of MSE estimated with the traditional and proposed methods. In particular, Figure 11(a) shows the result in the azimuth direction, and Figure 11(b) depicts the results in the slant-range direction. Notably, we only compared the 2D displacement time series during the period of August 2007 to March 2011 due to the fact that the traditional method fails to generate long-term displacement time series. From Figure 11(a) and (b), we can clearly see that the MSE of the 2D displacement time series estimated with the proposed method in both the azimuth and slant-range directions were less than 0.75 m, well within the range of the SAR offset tracking precision at 1/10–1/30 pixels [8,9]. However, the displacement time series estimated using the traditional method had much higher uncertainties, even exceeding 1.5 m in the slant-range

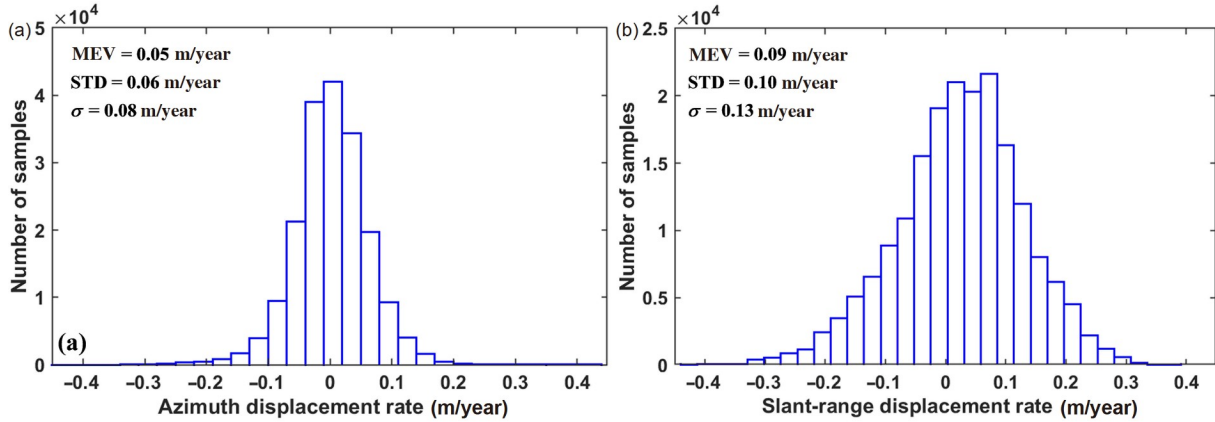


Figure 10 Histograms of the displacement rates in the azimuth (a) and slant-range (b) directions in the landslide-free areas, derived from the ALOS/PALSAR-1 and ALOS/PALSAR-2 images between August 2007 and May 2020.

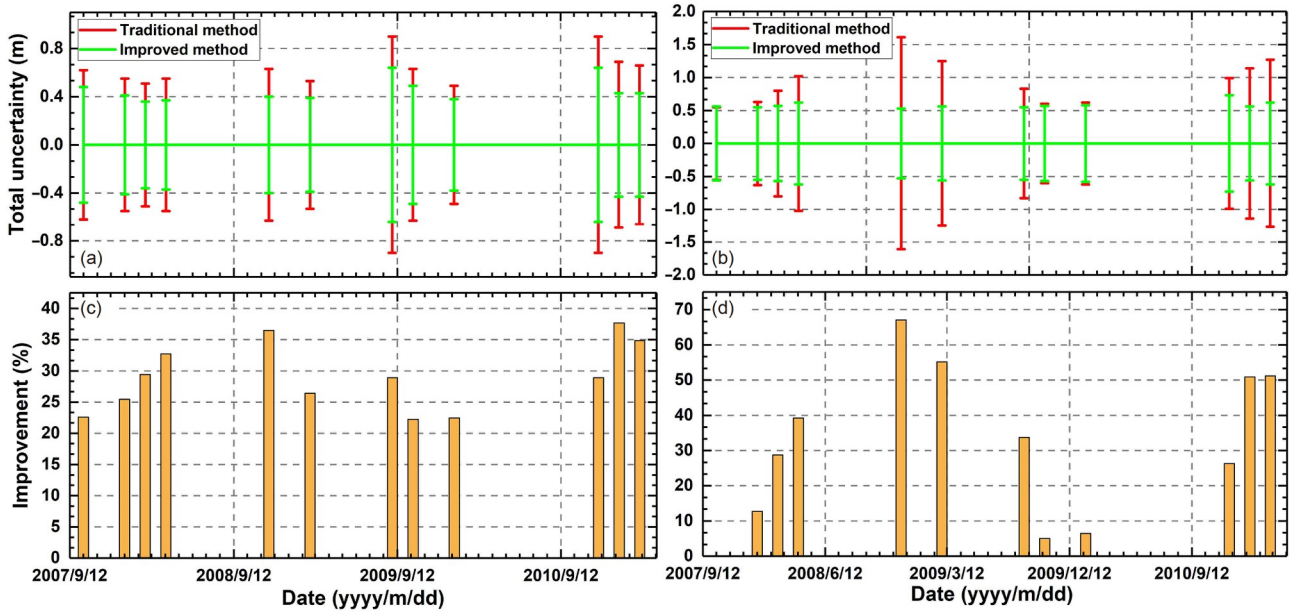


Figure 11 Total measurement uncertainties (MSE) of the 2D displacement time series for the ALOS/PALSAR-1 images in the landslide-free areas, calculated with the traditional (red lines) and improved (green lines) methods: (a) azimuth direction, (b) slant-range direction. The improvement percentages in uncertainties using the proposed methods: (c) azimuth direction, (d) slant-range direction.

direction in some SAR acquisitions. To better illustrate the improvement of our proposed method, we calculated the reduced percentage of uncertainties in the 2D displacement time series, as presented in Figure 11(c) and (d). Compared with the traditional method, the proposed method, on average, decreased the uncertainties by 30% and 31% in the azimuth and slant-range directions, respectively.

6 Discussion

6.1 Spatial deformation patterns revealed by horizontal movement vectors

The 3D displacement results provide a fine-scale description

of the real movements of the Laojingbian landslide, thus providing us with a better understanding of the spatial deformation patterns of the landslide. Therefore, we inverted the movement direction for each pixel of the landslide using the N-S and E-W displacement rates, as shown in Figure 12. Figure 12(a) shows a 3D view of the Laojingbian landslide, in which geomorphological features, such as gullies and unstable regions, are marked with lines of different colors. Figure 12(b) shows the horizontal movement vectors from August 2007 to March 2011, estimated using ALOS/PALSAR-1 images. Figure 12(c) shows the horizontal components from September 2014 to May 2020, calculated using the ALOS/PALSAR-2 images, and Figure 12(d) shows the horizontal displacements from August 2007 to May 2020,

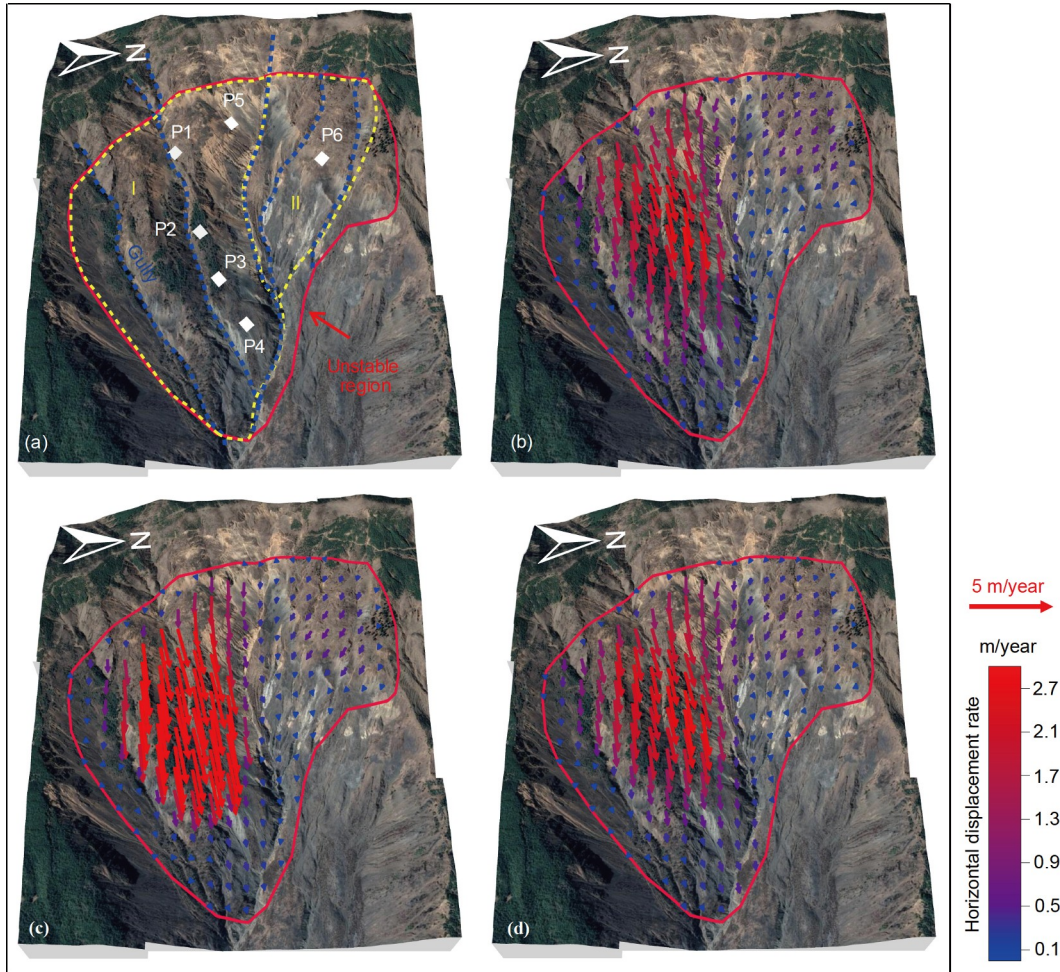


Figure 12 (a) Sketch of unstable blocks (indicated with Roman numbers I and II) of the Laojingbian landslide; (b) 2D vectors of the horizontal displacement of the Laojingbian landslide from August 2007 to March 2011; (c) 2D vectors of the horizontal displacement from September 2014 to May 2020; (d) 2D vectors of the horizontal displacement from August 2007 to May 2020.

estimated using the ALOS/PALSAR-1 and ALOS/PALSAR-2 images. On the basis of geomorphological analysis (Figure 12(a)), combined with the horizontal movement vectors presented in Figure 12(b), (c), and (d), we partitioned the entire active part of the Laojingbian landslide into two blocks of different deformation patterns and movement directions. Block I and Block II are labeled with yellow dotted lines in Figure 12(a). Block I is dominated by eastward movement, with an azimuth of approximately 78° – 85° . Evidence from geomorphological analysis (Figure 12(a)) and the slope aspect derived from DEM suggest that Block I is an east-oriented slope. In comparison, Block II is dominated by southeast movement, with an azimuth of approximately 115° – 125° . Its geomorphological features and slope aspect illustrate that Block II is a southeast-facing slope. The movement direction of the Laojingbian landslide retrieved from SAR-derived 3D displacements is highly consistent with that derived from geomorphological analysis, demonstrating the reliability of the estimated 3D displacements to some extent. Moreover, the movement rate of Block I is

much greater than that of Block II, thus indicating that Block I is the main sliding area of the slope with the largest horizontal displacement.

6.2 Kinematic modeling and early warning using 3D displacement time series

As shown in Figures 7 and 9, the long-term displacement time series retrieved from the cross-platform ALOS/PALSAR-1 and ALOS/PALSAR-2 images exhibited dominant acceleration signals of the Laojingbian landslide after February 13, 2015, indicating that the landslide seemed to have entered the accelerative displacement stage after this date. Evidence from Figure 12 demonstrates that the Laojingbian landslide movement is dominated by eastward displacement. Thus, we produced the horizontal displacement time series of P2 (marked in Figure 12(a)) from August 2007 to May 2020 through the synthesis of its E-W and N-S displacement time series (presented in Figure 9(b)), as shown in Figure 13 with the blue triangles. In Figure 13, we can divide the entire

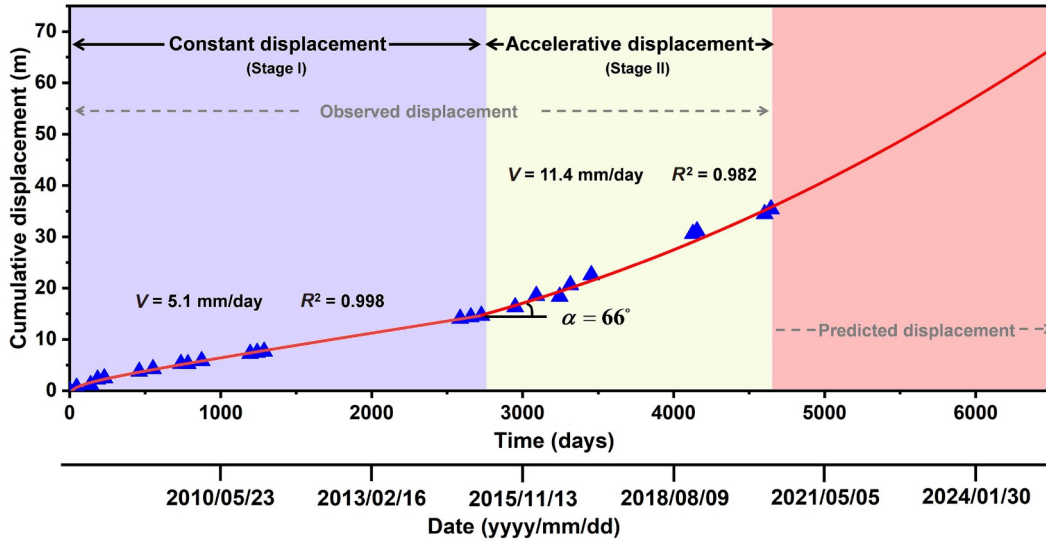


Figure 13 Modeling and prediction of landslide displacement using 3D displacement time series (for P2 marked in Figure 12(a)) from August 2007 to May 2020, shown in Figure 9(b). The blue triangles are the horizontal displacements observed using the ALOS/PALSAR-1 and ALOS/PALSAR-2 images, while the red line represents the modeled (within the purple and yellow columns) and predicted displacements (within the light red column). In addition, V , R^2 , and α represent the average horizontal displacement rate of the landslide, the coefficient of determination for displacement modeling, and the tangential angle of the displacement-time curve, respectively.

displacement time series into two stages: the displacement (Stage I) from August 27, 2007, to February 13, 2015, and the displacement (Stage II) from February 13, 2015, to May 15, 2020. Notably, a similar displacement evolution behavior was captured at P1, P2, P3, and P5, while point P2 had the largest cumulative displacement (Figures 7 and 9). Therefore, we chose an exemplary point of P2 for further analysis. The displacement rates in Stages I and II were approximately 5.1 and 11.4 mm/day, respectively. Fan et al. [50] developed a landslide early warning model by considering the changes in the displacement rate measured from *in situ* instruments, such as GNSS and crack gauges, as shown in eq. (S1). Consequently, on the basis of the estimated long-term displacement time series, we applied this model to issue an early warning of the Laojingbian landslide. The tangential angle (α) of the displacement-time curve in Stage II was calculated using eq. (S1) with a value of 66° . According to the guidelines and the threshold for α in landslide early warning previously established by geologists [50–53], the result suggested that the Laojingbian landslide had entered the accelerative displacement stage (Stage II) starting on February 13, 2015, and then entered the constant displacement stage (Stage I) before this date, with a constant movement rate. The value of α lies in the interval of 45° – 80° , suggesting that the period from February 2015 to May 15, 2020 (i.e., Stage II) can be categorized as the initial accelerative displacement stage. Therefore, a yellow warning (caution level) should be issued to the Laojingbian landslide, based on the warning criteria of landslides reported by Fan et al. [50] and Ju et al. [51].

The temporal evolution of landslides can be characterized using the unidimensional constitutive models of rocks. Based on laboratory testing of rocks with various materials [54], researchers have developed a series of unidimensional constitutive laws to model landslide displacements, as shown in eqs. (S2) and (S3), in which the former is suitable for modeling landslide movement at the constant displacement stage, whereas the latter is applied to model landslide movements at the accelerative displacement stage. Thus, we introduced eqs. (S2) and (S3) to model the observed displacement time series of Stages I and II of the Laojingbian landslide, respectively, as shown by the red line in Figure 13. We noticed that the unidimensional constitutive laws of the rocks perfectly modeled the displacement observed by cross-platform SAR images, with correlation coefficients greater than 0.98 for both stages. Next, we predicted the horizontal displacement of the Laojingbian landslide and its evolution in the following five years using the established model by unidimensional constitutive laws and the observed displacement. The results are indicated by the red curve within the light red rectangle in Figure 13. The results suggest that the Laojingbian landslide will experience dramatic displacement in the following five years and that the cumulative displacement in the horizontal direction may reach 66 m on May 14, 2025, in the natural deformation state. It is worth noting that this prediction could be affected by heavy rainfall and strong earthquakes. Thus, near real-time monitoring, forecasting, and early warning of the landslide should be adopted by combining the physical models of rocks (e.g., eqs. (S1), (S2), and (S3)), as well as the measurements from

in situ instruments (e.g., GNSS and crack gauges) and the SAR offset tracking and InSAR techniques.

6.3 Possible factors influencing the Laojingbian landslide activity

The results presented in Figure 13 illustrate that the landslide displacements measured by SAR images approach the results of the unidimensional constitutive models of the rocks, indicating that the Laojingbian landslide is a gravitational sliding slope [54]. However, some discrepancies have been noted between the observed and the modeled displacements in some SAR acquisitions, suggesting that the landslide activity may be impacted by external triggering factors. At the same time, identifying the primary triggering factor of landslides is crucial for successfully issuing early warnings. Therefore, we collected data on historical earthquakes that occurred within 250 km of the study area with a magnitude of $> M_s$ 4.0 and analyzed the relevance between seismic events as well as the landslide displacement time series and the residuals with respect to the modeled values. As presented in Figure 14, a strong earthquake event, namely, the Ludian earthquake (M_s 6.5), happened on August 3, 2014, in the study area, whose epicenter was approximately 110 km away from this landslide. We can clearly see that the landslide displacement accelerated six months after the Ludian earthquake event. Seismic shaking can weaken slopes across the landscape and make them more prone to slide with delay times of days to years after the earthquake [55]. Thus, the Ludian earthquake and subsequent aftershocks may have triggered an external impulse on the Laojingbian landslide. Moreover, we can also see from Figure 14 that the residual is strongly correlated with the earthquake activity when its

magnitude is larger than M_s 5.0 in the accelerative displacement stage. Therefore, there is strong evidence indicating that seismic activities can accelerate the displacement of the Laojingbian landslide, even low-magnitude earthquakes ($\sim M_s$ 5.0). A previous study [56] also found evidence based on InSAR observations that a low-magnitude earthquake (M_s 5.1) can increase the activity of landslides. Additionally, according to Keefer [57], an earthquake with a magnitude similar to that of the Ludian event can trigger coherent landslides at distances of over 100 km from the epicenter or fault rupture. In this study, as shown in the optical image in Figure 12(a), serious disruptions and tensile cracks existed on the ground surface of the Laojingbian landslide. There is evidence of extensive cracking and disruption of slopes as a result of earthquakes [50]. Thus, the early warning model of the Laojingbian landslide should be able to assimilate the impact of earthquakes with magnitudes larger than M_w 5.0 in further studies.

7 Conclusions

InSAR methods are usually infeasible for mapping the landslide displacement with a large gradient, while the traditional SAR offset tracking method is unable to map the landslide displacement between SAR images with larger spatiotemporal baselines. Therefore, in this study, we propose an improved SAR offset tracking method to reliably and efficiently retrieve the multi-dimensional and long-term time series displacement of landslides in areas with complex geomorphological and environmental conditions. Our method comprises three procedures: (1) ortho-rectification and accurate co-registration of SAR images, (2) optimal

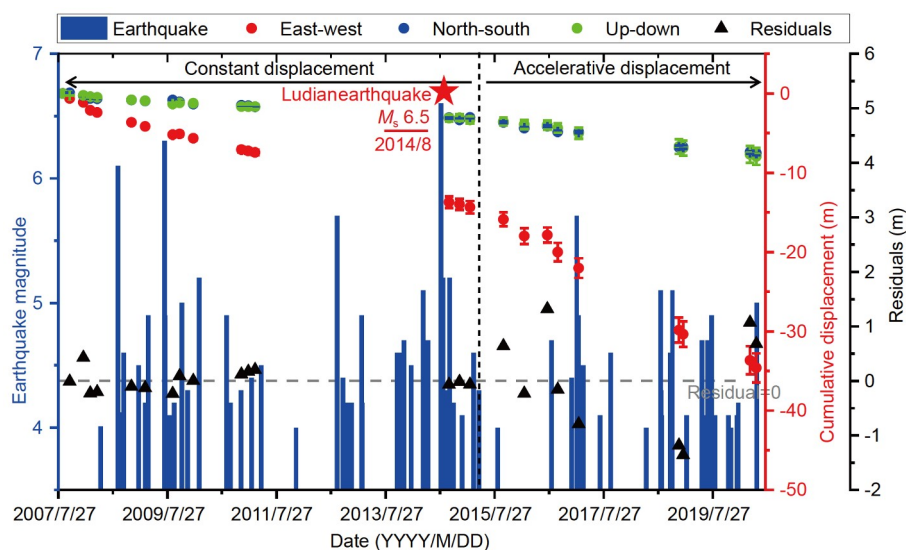


Figure 14 Relevance analysis between 3D landslide displacement time series at P2 marked in Figure 12(a) and earthquake events. Residuals indicate the differences between the observed displacement by SAR offsets and the one modeled using eqs. (S2) and (S3).

selection of offset pairs and cross-correlation calculation, and (3) estimation of the 2D and 3D displacement time series. The advantages of the proposed method were verified through analyses of the Laojingbian landslide, Jinsha River, China. The results show that the new method can estimate the landslide displacements in two (azimuth and slant-range directions) and three (N-S, E-W, and U-D directions) dimensions using the SAR observations, not only from an identical platform but also from cross-platforms, such as the ALOS/PALSAR-1 and ALOS/PALSAR-2 sensors. The major findings and contributions are summarized as follows.

The results derived from offset pairs with larger spatio-temporal baselines and cross-platforms demonstrated that the proposed method can effectively remove the systematic errors caused by topographic relief and largely improve the cross-correlation values of the long baseline offset pairs. Furthermore, the total measurement uncertainty was reduced by more than 70% for the displacement results calculated with longer spatiotemporal baseline pairs from an identical platform. With regard to the pairs from the cross-platform, our method can retrieve the 2D displacements successfully; in contrast, the traditional method fails to estimate the displacements.

The results from the simulated experiment and real data suggest that the proposed 2D displacement inversion method can efficiently restrain observational outliers. The 2D and 3D long-term time series displacements from August 2007 to May 2020 successfully revealed the deformation patterns and characteristics of the Laojingbian landslide, well approaching the modeled curve by unidimensional constitutive laws of rocks. Compared with the traditional method, our method largely decreases the measurement uncertainty in the estimated displacements, with an average improvement percentage of 30% in both the azimuth and slant-range directions.

The 3D displacement field also reveals that the Laojingbian landslide is an east-oriented slope consisting of two active blocks. The landslide deformation is driven by the force of gravity, whose movement is accelerated significantly by seismic events with a magnitude greater than M_s 5.0. Furthermore, the nearly 13 years' worth of displacement results illustrate that the Laojingbian landslide is currently in the onset of the accelerative displacement stage. Therefore, by combining long-term time series SAR offset tracking observations and early warning criteria for landslides, we recommend that a yellow warning (caution level) must be issued for the landslide. Thus, this research provides a new tool and insightful approach for the issuance of early warnings regarding catastrophic landslide hazards. It could also serve as a reference for cases of rapid slope deformation and failures in other regions.

China (Grant Nos. 41874005 and 41929001), the Fundamental Research Funds for the Central Universities, CHD (Grant Nos. 300102269712 and 300102269303), and by the China Geological Survey Projects (Grant Nos. DD20190637 and DD20190647). This research was also supported by a Chinese Scholarship Council studentship awarded to Xiaojie Liu (Grant No. 202006560031). The figures involved in this study were prepared using the following software: Matlab R2021a, GMT, ArcGIS, and Python.

Supporting Information

The supporting information is available online at tech.scichina.com and link.springer.com. The supporting materials are published as submitted, without typesetting or editing. The responsibility for scientific accuracy and content remains entirely with the authors.

- 1 Froude M J, Petley D N. Global fatal landslide occurrence from 2004 to 2016. *Nat Hazards Earth Syst Sci*, 2018, 18: 2161–2181
- 2 Li M H, Zhang L, Shi X G, et al. Monitoring active motion of the Guobu landslide near the Laxiwa Hydropower Station in China by time-series point-like targets offset tracking. *Remote Sens Environ*, 2019, 221: 80–93
- 3 Shi X, Liao M, Li M, et al. Wide-area landslide deformation mapping with multi-path ALOS PALSAR data stacks: A case study of Three Gorges Area, China. *Remote Sens*, 2016, 8: 136
- 4 Wasowski J, Bovenga F. Investigating landslides and unstable slopes with satellite multi temporal interferometry: Current issues and future perspectives. *Eng Geol*, 2014, 174: 103–138
- 5 Liu X, Zhao C, Zhang Q, et al. Integration of Sentinel-1 and ALOS/PALSAR-2 SAR datasets for mapping active landslides along the Jinsha River corridor, China. *Eng Geol*, 2021, 284: 106033
- 6 Singleton A, Li Z, Hoey T, et al. Evaluating sub-pixel offset techniques as an alternative to D-InSAR for monitoring episodic landslide movements in vegetated terrain. *Remote Sens Environ*, 2014, 147: 133–144
- 7 Dille A, Kervyn F, Handwerker A L, et al. When image correlation is needed: Unravelling the complex dynamics of a slow-moving landslide in the tropics with dense radar and optical time series. *Remote Sens Environ*, 2021, 258: 112402
- 8 Casu F, Manconi A, Pepe A, et al. Deformation time-series generation in areas characterized by large displacement dynamics: The SAR amplitude pixel-offset SBAS technique. *IEEE Trans Geosci Remote Sens*, 2011, 49: 2752–2763
- 9 Zhao C Y, Lu Z, Zhang Q. Time-series deformation monitoring over mining regions with SAR intensity-based offset measurements. *Remote Sens Lett*, 2013, 4: 436–445
- 10 Hu X, Wang T, Liao M S. Measuring coseismic displacements with point-like targets offset tracking. *IEEE Geosci Remote Sens Lett*, 2014, 11: 283–287
- 11 Hu J, Li Z W, Li J, et al. 3-D movement mapping of the alpine glacier in Qinghai-Tibetan Plateau by integrating D-InSAR, MAI and offset-tracking: Case study of the Dongkemadi Glacier. *Global Planet Change*, 2014, 118: 62–68
- 12 Wang T, Jónsson S. Improved SAR amplitude image offset measurements for deriving three-dimensional coseismic displacements. *IEEE J Sel Top Appl Earth Observ Remote Sens*, 2015, 8: 3271–3278
- 13 Yang Z F, Li Z W, Zhu J J, et al. An alternative method for estimating 3-D large displacements of mining areas from a single SAR amplitude pair using offset tracking. *IEEE Trans Geosci Remote Sens*, 2018, 56: 3645–3656
- 14 Shi X, Zhang L, Zhou C, et al. Retrieval of time series three-dimensional landslide surface displacements from multi-angular SAR observations. *Landslides*, 2018, 15: 1015–1027
- 15 Schaefer L N, Wang T, Escobar-Wolf R, et al. Three-dimensional displacements of a large volcano flank movement during the May 2010 eruptions at Pacaya Volcano, Guatemala. *Geophys Res Lett*, 2017, 44: 135–142

- 16 Chen L, Zhao C, Li B, et al. Deformation monitoring and failure mode research of mining-induced Jianshanying landslide in karst mountain area, China, with ALOS/PALSAR-2 images. *Landslides*, 2021, 18: 2739–2750
- 17 Sansosti E, Berardino P, Manunta M, et al. Geometrical SAR image registration. *IEEE Trans Geosci Remote Sens*, 2006, 44: 2861–2870
- 18 Sun L, Muller J P, Chen J. Time series analysis of very slow landslides in the three Gorges Region through small baseline SAR offset tracking. *Remote Sens*, 2017, 9: 1314
- 19 Scambos T A, Dutkiewicz M J, Wilson J C, et al. Application of image cross-correlation to the measurement of glacier velocity using satellite image data. *Remote Sens Environ*, 1992, 42: 177–186
- 20 Strozzi T, Luckman A, Murray T, et al. Glacier motion estimation using SAR offset-tracking procedures. *IEEE Trans Geosci Remote Sens*, 2002, 40: 2384–2391
- 21 Zhang L, Ding X, Lu Z. Ground settlement monitoring based on temporarily coherent points between two SAR acquisitions. *ISPRS J Photogramm Remote Sens*, 2011, 66: 146–152
- 22 Li M H, Zhang L, Ding C, et al. Retrieval of historical surface displacements of the Baige landslide from time-series SAR observations for retrospective analysis of the collapse event. *Remote Sens Environ*, 2020, 240: 111695
- 23 Liu X, Zhao C, Zhang Q, et al. Deformation of the Baige landslide, Tibet, China, revealed through the integration of cross-Platform ALOS/PALSAR-1 and ALOS/PALSAR-2 SAR observations. *Geophys Res Lett*, 2020, 47: e86142
- 24 Ansari H, De Zan F, Parizzi A. Study of systematic bias in measuring surface deformation with SAR interferometry. *IEEE Trans Geosci Remote Sens*, 2021, 59: 1285–1301
- 25 Bontemps N, Lacroix P, Doin M P. Inversion of deformation field time-series from optical images, and application to the long term kinematics of slow-moving landslides in Peru. *Remote Sens Environ*, 2018, 210: 144–158
- 26 Yang L, Zhao C, Lu Z, et al. Three-dimensional time series movement of the Cuolangma glaciers, southern Tibet with sentinel-1 imagery. *Remote Sens*, 2020, 12: 3466
- 27 Ali E, Xu W B, Ding X L. Improved optical image matching time series inversion approach for monitoring dune migration in North Sinai Sand Sea: Algorithm procedure, application, and validation. *ISPRS J Photogramm Remote Sens*, 2020, 164: 106–124
- 28 Seemkooei A A. Comparison of reliability and geometrical strength criteria in geodetic networks. *J Geodesy*, 2001, 75: 227–233
- 29 Handwerker A L, Booth A M, Huang M H, et al. Inferring the sub-surface geometry and strength of slow-moving landslides using 3-D velocity measurements from the NASA/JPL UAVSAR. *J Geophys Res Earth Surf*, 2021, 126: e05898
- 30 Hu J, Li Z W, Ding X L, et al. Resolving three-dimensional surface displacements from InSAR measurements: A review. *Earth-Sci Rev*, 2014, 133: 1–17
- 31 Mohr J J, Reeh N, Madsen S N. Three-dimensional glacial flow and surface elevation measured with radar interferometry. *Nature*, 1998, 391: 273–276
- 32 Ao M, Zhang L, Shi X, et al. Measurement of the three-dimensional surface deformation of the Jiaju landslide using a surface-parallel flow model. *Remote Sens Lett*, 2019, 10: 776–785
- 33 Huber P J. Robust estimation of a location parameter. *Ann Math Statist*, 1964, 35: 73–101
- 34 Lu Z, Dzurisin D. Ground surface deformation patterns, magma supply, and magma storage at Okmok volcano, Alaska, from InSAR analysis: 2. Coeruptive deflation, July–August 2008. *J Geophys Res*, 2010, 115: B00B03
- 35 Li J, Li Z, Ding X, et al. Investigating mountain glacier motion with the method of SAR intensity-tracking: Removal of topographic effects and analysis of the dynamic patterns. *Earth-Sci Rev*, 2014, 138: 179–185
- 36 Bamler R. Interferometric stereo radargrammetry: Absolute height determination from ERS-ENVISAT interferograms. In: *Proceedings of the International Geoscience and Remote Sensing Symposium 2000*. Honolulu, 2000. 742–745
- 37 Ding C, Zhang L, Liao M S, et al. Quantifying the spatio-temporal patterns of dune migration near Minqin Oasis in northwestern China with time series of Landsat-8 and Sentinel-2 observations. *Remote Sens Environ*, 2020, 236: 111498
- 38 Koblet T, Gärtner-Roer I, Zemp M, et al. Reanalysis of multi-temporal aerial images of Storgläciären, Sweden (1959–99)—Part 1: Determination of length, area, and volume changes. *Cryosphere*, 2010, 4: 333–343
- 39 Amiri-Simkooei A R, Asgari J, Zangeneh-Nejad F, et al. Basic concepts of optimization and design of geodetic networks. *J Surv Eng*, 2012, 138: 172–183
- 40 Fialko Y, Simons M, Agnew D. The complete (3-D) surface displacement field in the epicentral area of the 1999 M_w 7.1 Hector Mine Earthquake, California, from space geodetic observations. *Geophys Res Lett*, 2001, 28: 3063–3066
- 41 Samsonov S, Dille A, Dewitte O, et al. Satellite interferometry for mapping surface deformation time series in one, two and three dimensions: A new method illustrated on a slow-moving landslide. *Eng Geol*, 2020, 266: 105471
- 42 Golub G H, van Loan C F. An analysis of the total least squares problem. *SIAM J Numer Anal*, 1980, 17: 883–893
- 43 Eckart C, Young G. The approximation of one matrix by another of lower rank. *Psychometrika*, 1936, 1: 211–218
- 44 Mirsky L. Symmetric gauge functions and unitarily invariant norms. *Quart J Math*, 1960, 11: 50–59
- 45 Wang G, Xie M, Chai X, et al. D-InSAR-based landslide location and monitoring at Wudongde hydropower reservoir in China. *Environ Earth Sci*, 2013, 69: 2763–2777
- 46 Zhao C, Kang Y, Zhang Q, et al. Landslide identification and monitoring along the Jinsha River Catchment (Wudongde Reservoir Area), China, using the InSAR method. *Remote Sens*, 2018, 10: 993
- 47 Cai Y J, Cheng H Y, Wu S F, et al. Breaches of the Baige Barrier Lake: Emergency response and dam breach flood. *Sci China Tech Sci*, 2020, 63: 1164–1176
- 48 Necsoiu M, Leprince S, Hooper D M, et al. Monitoring migration rates of an active subarctic dune field using optical imagery. *Remote Sens Environ*, 2009, 113: 2441–2447
- 49 Crosetto M, Monserrat O, Cuevas-González M, et al. Persistent scatterer interferometry: A review. *ISPRS J Photogramm Remote Sens*, 2016, 115: 78–89
- 50 Fan X, Xu Q, Alonso-Rodríguez A, et al. Successive landsliding and damming of the Jinsha River in eastern Tibet, China: Prime investigation, early warning, and emergency response. *Landslides*, 2019, 16: 1003–1020
- 51 Ju N P, Huang J, He C Y, et al. Landslide early warning, case studies from Southwest China. *Eng Geol*, 2020, 279: 105917
- 52 Xu Q, Peng D, Zhang S, et al. Successful implementations of a real-time and intelligent early warning system for loess landslides on the Heifangtai terrace, China. *Eng Geol*, 2020, 278: 105817
- 53 Zhou X P, Ye T. Inverse-square-root-acceleration method for predicting the failure time of landslides. *Sci China Tech Sci*, 2021, 64: 1127–1136
- 54 Aydan Ö, Ito T, Özbay U, et al. ISRM suggested methods for determining the creep characteristics of Rock. *Rock Mech Rock Eng*, 2014, 47: 275–290
- 55 Fan X M, Scaringi G, Korup O, et al. Earthquake-induced chains of geologic hazards: Patterns, mechanisms, and impacts. *Rev Geophys*, 2019, 57: 421–503
- 56 Martino S, Fiorucci M, Marmoni G M, et al. Increase of landslide activity after a low magnitude earthquake inferred by DInSAR interferometry. *Res Square*, 2021, doi: 10.21203/rs.3.rs-785753/v1
- 57 Keefer D K. Landslides caused by earthquakes. *Geol Soc Am Bull*, 1984, 95: 406–421